ADVANCED ENERGY MATERIALS
www.advenergymat.de

Tri-Metallic Catalyst for Oxygen Evolution Reaction Enables Continuous Operation of Anion Exchange Membrane Electrolyzer at 1A cm^{-2} for Hundreds of Hours

Ali Abdelhafiz, Mona H. Mohammed, Jehad Abed, Dong-Chan Lee, Mengjie Chen, Ahmed S. Helal, Zhichu Ren, Faisal Alamgir, Edward Sargent, Paul A. Kohl, Sameh K. Elsaidi,* and Ju Li**

Although numerous efforts are made to synthesize active electrocatalysts for green hydrogen production; catalyst stability, and facile synthesis to scale up the production are still challenging. Herein, the production of novel non-PGM catalysts for the oxygen reduction reaction (OER) in an alkaline aqueous medium is reported, which is based on the synthesis of a trimetallic metal–organic framework (MOF) precursors. Fine-tuning of the composition of the metal centers (Ni, Co, and Fe) shows a great effect on OER activity after the MOF undergoes dynamic chemical and structural transformations under OER conditions. In situ characterization reveals the origin of OER activity enhancement as metals' oxidation state increases, inducing compressive mechanical strain on metal centers, enhancing the electronic conductivity through the formation of oxygen vacancies, and stronger metal–oxygen covalency. Catalysts are used in membrane electrode assembly (MEA) setup within an industrial full-cell anion exchange membrane electrolyzer (AEMEC), showing a stable performance for 550 h without noticeable decay at 750 and 1000 mA cm^{-2} industrial level current densities.

1. Introduction

The carbon net-zero target by 2050 demands CO_2-free energy resources such as wind, nuclear energy, and solar photovoltaics, which promise to generate electricity in abundance. However, grid-scale battery storage has a storage capacity limited to just a few hours.[1] Therefore, the conversion of that generated electricity into useful chemical fuels (e.g., H_2) is essential.[2–5] In this context, water electrolysis to generate green hydrogen has been the topic of interest where one needs to maximize the rate of H_2 production for prolonged periods at reduced cost. The electrochemical catalyst is a crucial factor that contributes to the performance, longevity, and cost of water electrolyzers.[6] Oxygen evolution reaction (OER) is the

---

A. Abdelhafiz, J. Li
Department of Nuclear Science and Engineering
Massachusetts Institute of Technology
77 Massachusetts Ave, Cambridge, MA 02139, USA
E-mail: ali_m@mit.edu; liju@mit.edu

M. H. Mohammed, S. K. Elsaidi
Department of Chemistry
Illinois Institute of Technology
Chicago, IL 60616, USA
E-mail: selsaidi@iit.edu

M. H. Mohammed, S. K. Elsaidi
SE-MAT Smartly Engineered Materials LLC
Pittsburgh, PA 15238, USA

The ORCID identification number(s) for the author(s) of this article can be found under https://doi.org/10.1002/aenm.202303350

© 2024 The Authors. Advanced Energy Materials published by Wiley-VCH GmbH. This is an open access article under the terms of the Creative Commons Attribution License, which permits use, distribution and reproduction in any medium, provided the original work is properly cited.

DOI: 10.1002/aenm.202303350

J. Abed
Department of Materials Science and Engineering
University of Toronto
Toronto, Ontario M5S 3G4, Canada

D.-C. Lee, F. Alamgir
School of Materials Science and Engineering
Georgia Institute of Technology
771 Ferst Dr NW, Atlanta, GA 30332, USA

D.-C. Lee
Department of Chemical Engineering
Hongik University
94 Wausan-ro Mapo-gu, Seoul 04066, Republic of Korea

M. Chen, P. A. Kohl
School of Chemical and Biomolecular and Engineering
Georgia Institute of Technology
311 Ferst Dr NW, Atlanta, GA 30332, USA

A. S. Helal
Department of Nano Engineering
Faculty of Nanotechnology for Postgraduate Studies
Sheikh Zayed Branch Campus
Cairo University
Sheikh Zayed City 12588, Egypt

16146840, 0, Downloaded from https://onlinelibrary.wiley.com/doi/10.1002/aenm.202303350 by Massachusetts Institute of Technolo, Wiley Online Library on [02/04/2024]. See the Terms and Conditions (https://onlinelibrary.wiley.com/terms-and-conditions) on Wiley Online Library for rules of use; OA articles are governed by the applicable Creative Commons License

more sluggish reaction that takes place at the positive electrode (i.e., anode) of the water electrolyzer, where a stable catalyst at an industrial level of current density, e.g. $1A/cm^2$, is a must.[7]

Proton exchange membrane electrolyzers (PEMEC) that operate at acidic conditions, however, rely on noble metals (Ir, or Ru) as the OER catalysts of choice.[7] The recent developments of robust and highly efficient anion exchange membrane (AEM) open the door to exploring the paradigm of non-noble metal catalysts for OER in anion exchange membrane electrolyzer cell (AEMEC). To maximize hydrogen production and optimize cost, operating the cell at higher current densities (e.g., > 500 mA cm^{-2}) is critical because the hydrogen generation rate is proportional to the cells' current density and the balance-of-plant cost requires this density to be high enough to be economical.[8,9] However, high current densities require a large operating potential (> 2 V) due to high electrochemical overpotentials for the sluggish OER and poor catalyst performance. In addition, at high current density, AEMEC suffers from short lifetimes (i.e., an order of magnitude shorter than the desired industrial lifespan) due partly to poor catalyst stability at extreme chemo-mechanical conditions.[10,11]

Multi-metallic catalysts (e.g., Co, Ni, Fe, and/or Mn) have shown great promise to catalyze OER in an alkaline aqueous medium.[12–16] Metal–organic frameworks (MOF) where metal ions are coordinated through organic ligands are versatile to host multiples of different atoms with almost infinite compositional variations.[17] Several binary MOFs of Ni-Fe, Fe-Co, and Ni-Co have been presented in literature while showing decent performance to catalyze OER.[18–20] Yet, the performance of those bimetallic MOFs and others falls short in terms of cost-effective replacement of noble metal catalysts because they are not stable in AEMEC for prolonged periods.[21] To date, the transition of outstanding lab-scale catalytic activity into an industrial-level setup (i.e., from 3-electrode setup to membrane electrode assemblies (MEA)) is a serious obstacle hampering the more widespread commercial adoption of AEMEC.[22] Moreover, the scientific understanding of the reasons behind activity enhancement or degradation retardation is lacking.[20,22,23]

Herein, we report the design of tri-metallic MOFs with non-noble metals to catalyze OER toward green H_2 production in AEMEC full cells. Several families of tri-metallic Fe-Ni-Co MOFs have been investigated for OER in an alkaline medium, to identify optimal composition with the highest power to catalyze OER, while maintaining stable performance for hundreds of hours at elevated current densities. Powered by in situ X-ray absorption spectroscopy (XAS) in conjunction with various electrochemical testing protocols, the origin of OER activity dependency has been investigated, correlated to the chemical state of transition metal centers (Fe, Ni, and Co) in addition to local atomistic structure in the vicinity of the metal center. The systematic analyses of the designed MOFs in correlation with their catalytic activity and stability, showed a great dependence on the dynamic structural and chemical transformations taking place under different stages of the OER process. AEMEC device testing showed very stable performance for hundreds of hours of continuous operation at elevated current density (750 and 1000 mA cm^{-2}) without notable decay in performance. The scientific and technological outcomes of the advance opens the door not only to cost-effective and highly efficient production of green hydrogen but may also carry over to other applications such as CO_2 capture and conversion.

2. Results

2.1. Synthesis and Structure

MOF-74(*M*) is a family of MOFs assembled by the coordination of metal cations (M = Mg, Ca, Co, Ni, Zn, Fe, Mn, Cu) and 2,5-dioxido-1,4-benzenedicarboxylate (DOBDC).[24–26] This MOF platform was chosen for the study due to its unique characteristic features: 1) The type and composition of the rod-shaped metal nodes can be readily modified, 2) the large one-dimensional hexagonal channel of the MOF-74 enables fast diffusion of reactants (i.e., it is open) so facile transformation can happen throughout the original structure under aggressive conditions, and 3) it contains highly accessible unsaturated metal centers (i.e., metal atoms are not fully surrounded with native oxygen from the ligand, which is maximizing the density of available active site to host reaction intermediates). We systematically changed the composition of three metals in MOF-74: Co, Ni, and Fe, which are known for their good catalytic aptitude for OER. In a Teflon autoclave, the metal salts are mixed in different ratios with the DOBDC ligand in a solvent mixture of dimethyl formamide (DMF), water, and ethanol, as discussed in detail in the Supporting Information (SI). The mixtures were then kept at 130 °C for 2 days. After cooling, the MOF powders were washed, solvent-exchanged, filtrated, and activated to obtain dry powders. The powder X-ray diffraction (XRD) showed that the spectra of all synthesized MOF-74 isostructural analogs have well-defined diffraction peaks, which are consistent with the simulated pattern of the crystalline MOF-74 structure (Figures S1–S4, Supporting Information). Inductively Coupled Plasma Mass Spectrometry (ICP-MS) results showed that the percentages of each metal in the final MOF structures were comparable to the ratios of the metal precursors used in the synthesis. **Figure 1** shows a diagram of the tri-metallic MOF-74 structure studied herein, viewed perpendicular to the hexagonal channel.

Three families of MOF-74 analogs were synthesized in the presented study herein. Each family assessed the effect of a given metal (i.e., Ni, Co, or Fe) on OER activity and corresponding structural and chemical properties. The total molar ratio of the three metals remained constant for all the studied analogs. For example, the effect of adding Ni to Fe and Co was studied by varying the Ni loading, while having Fe and Co loading equal (i.e., $Ni_{100\text{-}2x}Co_xFe_x$). In the same context, two additional families of ternary MOFs were synthesized while varying Fe with respect to Ni and Co, and another with varying Co with respect to Ni and Fe,

---

A. S. Helal
Nanotechnology and Advanced Materials Laboratory
Nuclear Materials Authority
3rd settlement 11936, Egypt
A. S. Helal, Z. Ren, J. Li
Department of Materials Science and Engineering
Massachusetts Institute of Technology
77 Massachusetts Ave, Cambridge, MA 02139, USA
E. Sargent
Department of Chemistry
Northwestern University
2145 Sheridan Road, Evanston, IL 60208, USA

© 2024 The Authors. Advanced Energy Materials published by Wiley-VCH GmbH

16146840, 0, Downloaded from https://onlinelibrary.wiley.com/doi/10.1002/aenm.202303350 by Massachusetts Institute of Technolo, Wiley Online Library on [02/04/2024]. See the Terms and Conditions (https://onlinelibrary.wiley.com/terms-and-conditions) on Wiley Online Library for rules of use; OA articles are governed by the applicable Creative Commons License

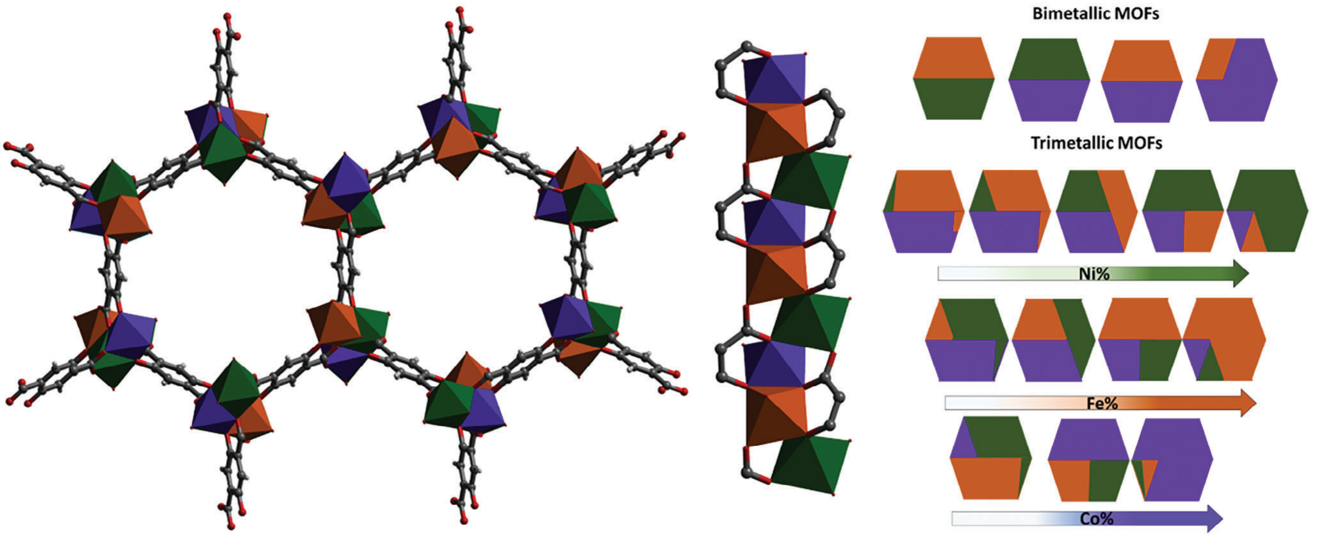

Figure 1. The left diagram shows a tri-metallic (Fe, Ni, and Co) MOF-74 structure. The schematic on the right shows the different combinations of the synthesized MOF-74 families: binary MOFs, and the three families of ternary MOFs. Ni, Fe, and Co are represented by green, brown, and purple colors, respectively.

as represented with the following formulas ($Fe_{100\text{-}2x}Ni_xCo_x$, and $Co_{100\text{-}2x}Ni_xFe_x$, respectively). A full list of the synthesized MOFs with their corresponding chemical compositions can be found in Table S1 (Supporting Information). As far as we can tell, these cations form a random solid solution (RSS) in the MOF lattice, without evidence of chemical long-range order. The presented innovative synthesis strategy sets our research apart, enabling large-scale production of MOF-74 with high purity and the generation of small nanoparticles. Unlike previous reports, where Fe-based MOF-74 variants often showed iron oxides due to the oxidation of Fe^{2+} to Fe^{3+}, our unique approach involved employing different metal counter ions.[27,28] In particular, we discovered that employing $FeSO_4$ as the source for Fe in the synthesis not only stabilizes Fe^{2+} but also leads to the formation of a pristine trimetallic MOF-74 with no impurities. Synthesis of impure analogs of MOF-74 would result in lower activity. In addition, homogeneity and purity of the catalysts are very critical to fabricate superior MEAs, due to poor electrode coating and sluggish mass transfer. Our synthesis strategy is facile and highly reproducible where several grams of the catalyst with high purity have been synthesized successfully. For example, one batch of 5 g catalyst is enough to fabricate 2500 cm^2 of MEA.

2.2. Electrocatalytic Activity Toward OER

Several combinations of metal centers were included in the synthesized MOFs (binary and ternary). Metal centers (Fe, Ni, and Co) are the metals of choice herein, due to their activity toward OER in aqueous alkaline medium.[16,19,29,30] Ratios of the different metals were modified systematically while observing the corresponding OER activity. All tests were conducted in 1 M KOH electrolyte. All experiments were performed in a deaerated (i.e., O_2-free) environment, by bubbling N_2 gas in the electrolyte for at least 45 min prior to any experiment. Reference and counter electrodes were chosen to be Hg/HgO and Pt foil, respectively. OER activity was probed by linear sweep voltammetry (LSV) at a scan rate of 5 mV s^{-1}. Increasing the chemical diversity of a catalytic system can sometimes induce a great enhancement in performance toward various electrocatalytic reactions, including OER, similarly in other electrocatalytic reactions (e.g., ORR).[12,13,31] **Figure 2** shows trends for various families of the synthesized ternary MOFs. Figure 2a shows the effect of modifying Ni concentration in the trimetallic NiCoFe MOF, while the concentration of both Fe and Co remain equal (i.e., $Ni_{100\text{-}2x}Co_xFe_x$). Figure 2a shows a dramatic effect of Ni addition to Co and Fe, where a monotonic decrease in OER activity was observed while increasing Ni content. The overpotential at 10 mA cm^{-2} was negatively affected when Ni percentage exceeded 33%, compared to commercial IrO_2 catalyst. It is worth noting that IrO_2 is not the catalyst of choice for alkaline OER. However, it has been used as a universal benchmark herein to evaluate the different catalysts because it is the preferred OER catalyst in acid conditions. Ni 5 and 10 wt.% concentrations showed enhancements in OER activity, where the overpotential at 10 mA cm^{-2} was lower by 70 and 40 mV, respectively, compared to IrO_2. MOF-74($Ni_5Co_{47.5}Fe_{47.5}$) showed an overpotential of 260 mV. It's worth mentioning that LSV curves shown in the study are not IR-compensated.

In a similar fashion, to assess the effect of Fe metal-center, Fe concentration was varied while the Ni and Co concentrations remained equal in each composition (i.e., $Fe_{100\text{-}2x}Ni_xCo_x$), as shown in Figure 2b. Reducing the Fe content showed a monotonic increase in the OER activity, whereas a Fe concentration of <50% showed a significant enhancement in OER activity compared to IrO_2. Samples with 10, 20, and 50 wt.% Fe showed an enhancement in overpotential compared to IrO_2 by 62, 59, and 30 mV, respectively. $Fe_{10}Ni_{45}Co_{45}$ showed an overpotential of 250 mV. Figure 2c depicts the effect of Co variation on OER activity. Co 10% concentration showed similar performance to the IrO_2 catalyst. On the other hand, increasing the Co concentration showed

© 2024 The Authors. Advanced Energy Materials published by Wiley-VCH GmbH

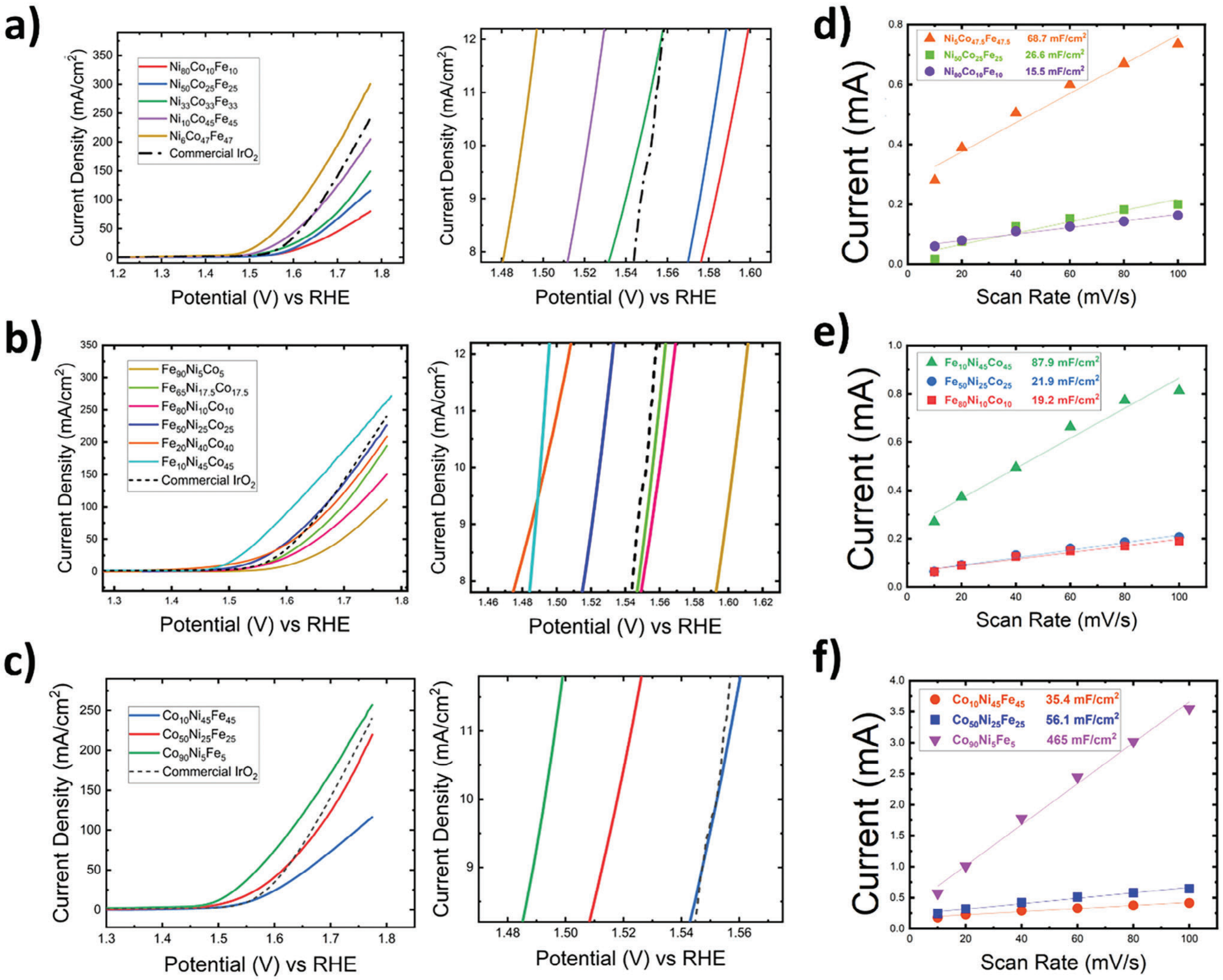

Figure 2. Electrochemical OER test probed in O_2-free 1 M KOH electrolyte. a–c) non-IR compensated LSV scans of the three MOF-74, with the right panel showing LSV scans at 10 mA cm^{-2} current density. d–f) Electrochemical active surface area (ECSA) of the families tested a–c, respectively. Families tested: a,d) $Ni_{100-2x}Co_xFe_x$, b,e) $Fe_{100-2x}Ni_xCo_x$, and c,f) $Co_{100-2x}Ni_xCo_x$.

further enhancement in OER activity. Co concentrations of 50 and 90%, showed an reduction in overpotential by 44 and 68 mV, respectively, compared to IrO_2.

In summary, decreasing the Ni content compared to Fe and Co showed an enhancement in activity. A similar observation is valid for Fe, where decreasing Fe loading in comparison to Ni and Co showed enhancement in activity. On the contrary, increasing Co concentration showed a positive effect on OER activity. The best MOF analog of each data set represented in Figure 2a–c is compared side-to-side, as shown in Figure S7 (Supporting Information). Comparing the overpotential at 10 mA cm^{-2} showed that the best performance is recorded by Ni deficient sample (i.e., $Ni_5Co_{47.5}Fe_{47.5}$), followed by Fe deficient sample (i.e., $Fe_{10}Ni_{45}Co_{45}$), while Co rich sample (i.e., $Co_{90}Ni_5Fe_5$) showed the largest overpotential among the three samples. At higher current densities, 100 mA cm^{-2}, Co rich sample still showed the largest overpotential among the three samples in comparison, while $Fe_{10}Ni_{45}Co_{45}$ showed the best activity. The aforementioned results imply that the OER activity of the synthesized MOFs is highly sensitive to chemical composition and applied potential (i.e., or corresponding current density), in agreement with other literature reports.[12,13,29,32–34]

To further understand the effect of different alloying compositions, the electrochemical active surface area (ECSA) has been evaluated from electrical double-layer capacitance (C_{dl}) for each sample. Double-layer capacitance is measured by running cyclic voltammetry (CV) scans at different scan rates (10, 20, 40, 60, 80 and 100 mV s^{-1}). The slope of the fitted straight line generated from plotting current density versus scan rate, at a given potential in the non-Faradaic region, represents the double-layer capacitance, which is proportional to ECSA (i.e., shallow slope infers a small double-layer capacitance, and small ECSA in return). Figure 2d–f shows the trends obtained from deducing double-layer capacitance at different scan rates for each sample set shown in Figure 2a–c, respectively. Considering Ni as the element of interest, by changing its concentration while

© 2024 The Authors. Advanced Energy Materials published by Wiley-VCH GmbH

16146840, 0, Downloaded from https://onlinelibrary.wiley.com/doi/10.1002/aenm.202303350 by Massachusetts Institute of Technolo, Wiley Online Library on [02/04/2024]. See the Terms and Conditions (https://onlinelibrary.wiley.com/terms-and-conditions) on Wiley Online Library for rules of use; OA articles are governed by the applicable Creative Commons License

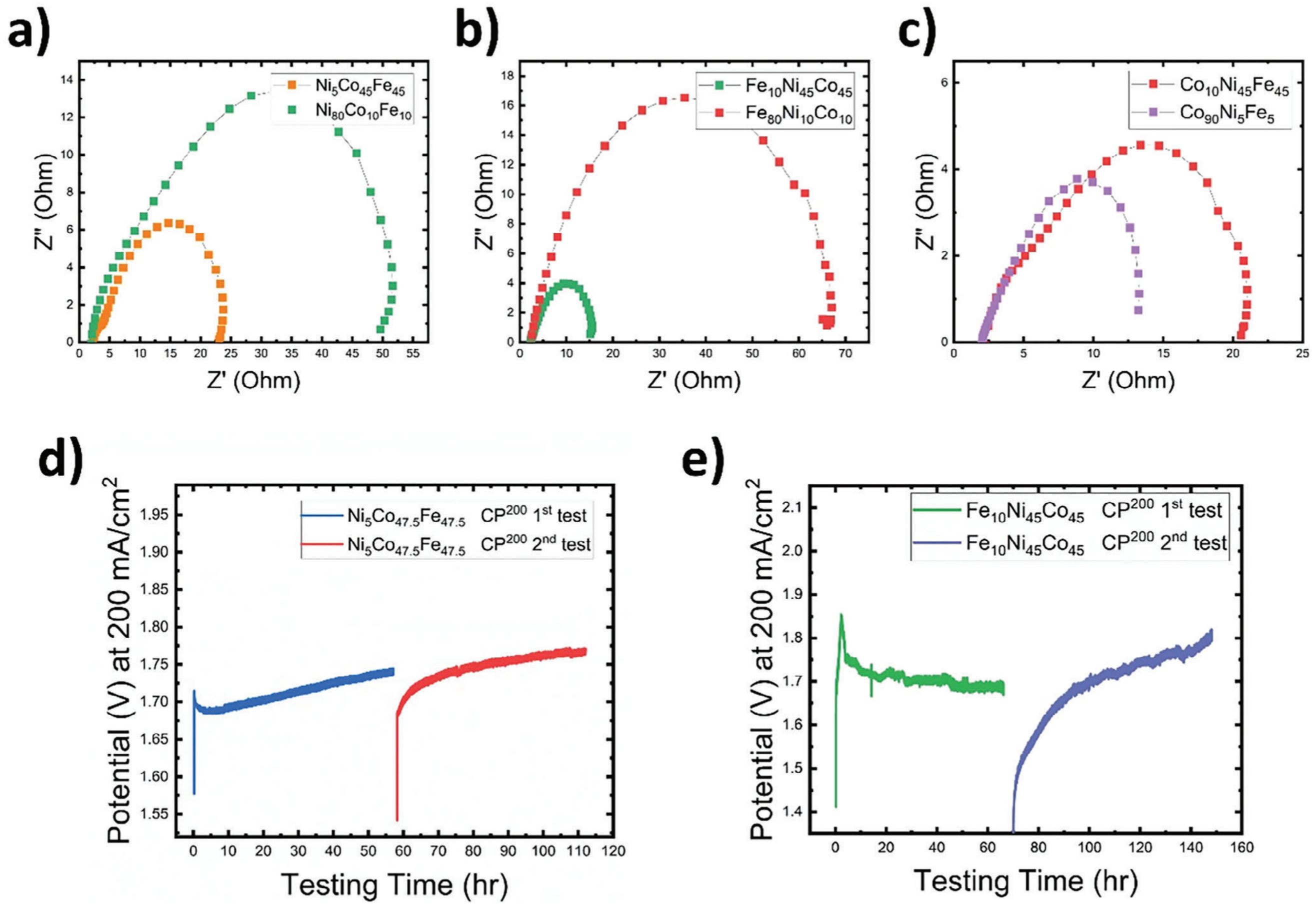

Figure 3. a–c) Nyquist plots depicting the electrochemical impedance trends of the different MOF-74 families in 1 M KOH electrolyte, at 1.65 V versus RHE reference electrode and frequency range of 200 KHz–100 mHz and 6 points per decade. Families tested: a) Ni$_{100\text{-}2x}$Co$_x$Fe$_x$, b) Fe$_{100\text{-}2x}$Ni$_x$Co$_x$, and c) Co$_{100\text{-}2x}$Ni$_x$Co$_x$. d,e) Stability testing under constant current modes, performed through chronopotentiometry at 200 mA cm^{-2} (CP^{200}). d) CP^{200} of Ni$_5$Co$_{47.4}$Fe$_{47.5}$ testing for 115 h total, divided into two segments separated by applying OCV for 1 h (blue and red, sequentially). e) CP^{200} of Fe$_{10}$Ni$_{45}$Co$_{45}$testing for 150 h total, divided into two segments separated by applying OCV for 1 h (green and purple, sequentially).

keeping the concentration of Fe and Co even for all compounds, Figure 2d shows that decreasing the Ni loading with respect to Fe and Co resulted in increasing ECSA. Ni$_5$Co$_{47.5}$Fe$_{47.5}$ showed a maximum ECSA of 68.7 mF cm^{-2}, compared to 26.6 and 15.5 for Ni$_{50}$Co$_{25}$Fe$_{25}$ and Ni$_{80}$Co$_{10}$Fe$_{10}$, respectively. This observation aligns with LSV trends shown in Figure 2a, where the activity increases with reducing the Ni loading. A larger surface area provides more catalytically active sites to catalyze OER.

Figure 2e shows the ECSA trends while investigating the effect of Fe loading, with respect to Ni and Co. ECSA deduced from C_{dl} showed that decreasing the Fe loading resulted in higher ECSA. Fe loading of 10, 50, and 80% in Fe$_{10}$Ni$_{45}$Co$_{45}$, Fe$_{50}$Ni$_{25}$Co$_{25}$, and Fe$_{80}$Ni$_{10}$Co$_{10}$, showed C_{dl} values of 87.9, 21.9, and 19.2 mF cm^{-2}, respectively. It is worth mentioning that ECSA trends quantified for both sample sets (i.e., Ni$_{100\text{-}2x}$Co$_x$Fe$_x$ and Fe$_{100\text{-}2x}$Ni$_x$Co$_x$) fall within the same range. This may suggest that both sets have a common factor influencing ECSA. Looking at the different compositions, it could be inferred that the Co ratio plays a vital role in the activity of the different catalysts while maximizing ECSA. Thus, Co loading was varied to investigate the role of Co on activity and stability. ECSA deduced from C_{dl} depicted in Figure 2f represents the data of Co$_{90}$Ni$_5$Fe$_5$, Co$_{50}$Ni$_{25}$Fe$_{25,}$ and Co$_{10}$Ni$_{45}$Fe$_{45}$. Results showed that increasing Co loading increases ECSA significantly. A sample with 90% Co (i.e., Co$_{90}$Ni$_5$Fe$_5$) showed an elevated C_{dl} of 465 mF cm^{-2}. Even though Co$_{90}$Ni$_5$Fe$_5$ obtained an order of magnitude larger ECSA than its counterparts (i.e., Ni$_5$Co$_{47.5}$Fe$_{47.5}$ and Fe$_{10}$Ni$_{45}$Co$_{45}$), its OER performance is marginally lower, as shown in Figure S7 (Supporting Information). This implies that while increasing the Co loading showed a tremendous influence on ECSA trends, it does not dictate the OER activity trend. This also indicates that the OER intrinsic activity (i.e., current density divided by ECSA) of Co$_{90}$Ni$_5$Fe$_5$ is much smaller than Ni$_5$Co$_{47.5}$Fe$_{47.5}$ and Fe$_{10}$Ni$_{45}$Co$_{45}$.

Electrochemical impedance spectroscopy (EIS) is used to study the reaction kinetics and charge transfer ability to differentiate the catalytic performance toward OER. **Figure 3** depicts Nyquist plots of different catalysts tested in oxygen-free 1 M KOH electrolyte. Samples were tested at 1.65 V versus RHE to probe the electrochemical reactivity at the vicinity of OER onset. EIS results aligned with LSV and ECSA trends shown in Figure 2a,d, where Ni-deficient catalyst (i.e., Ni$_{10}$Co$_{45}$Fe$_{45}$) showed a smaller

© 2024 The Authors. Advanced Energy Materials published by Wiley-VCH GmbH

16146840, 0, Downloaded from https://onlinelibrary.wiley.com/doi/10.1002/aenm.202303350 by Massachusetts Institute of Technolo, Wiley Online Library on [02/04/2024]. See the Terms and Conditions (https://onlinelibrary.wiley.com/terms-and-conditions) on Wiley Online Library for rules of use; OA articles are governed by the applicable Creative Commons License

semi-circle compared to Ni-rich catalyst (i.e., $Ni_{80}Co_{10}Fe_{10}$). A larger semi-circle (i.e., the difference between the low-frequency and high-frequency x-intercept) indicates more sluggish OER charge transfer kinetics, where the resistance of MOF $Ni_{80}Co_{10}Fe_{10}$ is almost double that of $Ni_{10}Co_{45}Fe_{45}$. Similarly, varying the content of Fe in MOF ($Fe_{100-2x}Ni_xCo_x$) had a large effect on EIS. Iron-rich analogs (i.e., $Fe_{80}Ni_{10}Co_{10}$) showed significantly more sluggish charge transfer kinetics compared to iron-deficient analogs (i.e., $Fe_{10}Ni_{45}Co_{45}$). Comparing the x-axis intercepts, the EIS of $Fe_{80}Ni_{10}Co_{10}$ is ≈430% compared to that of $Fe_{10}Ni_{45}Co_{45}$.

Nyquist plots shown in Figure 3c compare the effect of rich and poor Co analogs (i.e., $Co_{100-2x}Ni_xFe_x$). Results showed that increasing the Co-rich analog (i.e., $Co_{90}Ni_5Fe_5$) with 9 times larger Co loading, compared to $Co_{10}Ni_{45}Fe_{45}$, only enhanced the charge transfer kinetics (i.e., decreasing EIS) by the double. Those observations indicate that controlling the loading of Fe, followed by Ni, is of a significant importance in influencing the charge-transfer kinetics. On the other hand, increasing the Co loading to dominate the MOF composition did not result in a significant change in OER activity. Given the fact that Co prices (i.e., \$/kg) are two to three orders of magnitude more expensive compared to Fe, and more than double that of Ni, designing a highly active MOF with a reduced Co loading is of a great commercial value.

Catalyst stability is crucial for translating laboratory-scale results into device-level applications (e.g., AEMEC). Testing at a high current density is desirable to emulate the real performance of AEMEC. MOF stability was tested by applying a constant current of 200 mA cm^{-2} (chronopotentiometry (CP^{200})), while observing the potential change. Figure 3d shows the stability testing of $Ni_5Co_{47.4}Fe_{47.5}$ at CP^{200}. The sample was tested for 60 h, where the measured potential increased by 0.83 mV h^{-1}. The rapid increase in potential is due to accumulated gas bubbles at the electrode surface. Therefore, samples were kept at open circuit voltage (OCV) for 1 h after the first segment of testing finished (blue curve) to relieve the electrode from the gas bubble accumulation. Afterward, the same sample was subjected to another segment of stability testing (CP^{200}) to reach a total of 115 h. $Ni_5Co_{47.4}Fe_{47.5}$ samples showed tremendous stability where no potential jump was observed under harsh testing conditions (i.e., 200 mA cm^{-2}). Potential jump is an indication of a complete electrode deactivation (i.e., termination of OER activity), which is reported for IrO_2 commercial catalysts to be <1 h at similar testing conditions.[12,35,36] LSV scans performed before and after 115 h of testing showed a very interesting observation, where the overpotential is reduced with testing, as shown in Figure S8 (Supporting Information). This observation implies an enhancement in OER activity of $Ni_5Co_{47.4}Fe_{47.5}$ with time, which is believed to be due to structural and chemical activation of the catalyst under OER conditions, as will be discussed in the following section.

Under similar conditions, the $Fe_{10}Ni_{45}Co_{45}$ sample was tested as shown in Figure 3e. The first stability testing section was carried out for 70 h. At the start of the test, the potential increased from 1.68 to 1.85 V (vs RHE) within the first two hours of testing at CP^{200}. Afterward, the potential decreased to reach 1.75 V (vs RHE) during the 3rd–4th h of testing, as shown in (Figure S9, Supporting Information). Thereafter, for the remainder of the testing period, the potential profile was slightly decreased until reaching 1.695 V at the 70th h. This observation suggests that $Fe_{10}Ni_{45}Co_{45}$ went through a long activation process where structural and/or chemical transformation of the MOF and its metal center occurred to benefit the OER activity. The same sample was then kept at OCV for 1 h to release the gas bubbles accumulation at the surface, as described earlier. The second segment of stability testing at CP^{200} was carried out for an additional 80 h (i.e., $Fe_{10}Ni_{45}Co_{45}$ sample tested at CP^{200} for a total of 150 h).

2.3. Probing the Dynamic Chemical and Structural Perturbation Under OER Conditions

In situ X-ray absorption spectroscopy (XAS) was used to reveal the chemical and structural states of the synthesized MOFs under OER conditions. Measurements were performed in 1 M KOH electrolyte under fluorescence yield mode in an air-tight 3-electrode cell. The oxidation state (i.e., valence) of the different metal cations of MOF (i.e., Fe, Co, or Ni) influences the catalysts' activity and stability toward OER. The same sample was scanned at different OER testing conditions, labeled as dry, OCP, 1.1 V (vs RHE), and 1.5 V (vs RHE). Dry sample scans were performed on the as-synthesized powder. On the other hand, samples immersed in alkaline aqueous electrolytes in a 3-electrode configuration, without applied external bias, refer to open circuit potential (OCP). Additional XAS scans were performed for samples, while under external bias of 1.1 and 1.5 V versus RHE, referring to the sample before OER (i.e., pre-OER) and around OER onset, respectively.

Changes in electronic structure and oxidation state were probed by analyzing the X-ray absorption near-edge structure (XANES) spectra. Edge position and spectral structure of XANES indicate the extent of oxidation of a given element, where shifting to higher eV energies indicates an increase in the oxidation state (i.e., an increase of transition metals' valence) of that respective element. **Figure 4** shows in situ XAS spectra of the different elements in ternary NiCoFe MOF, and the in situ Co K-edge XANES is depicted in Figure 4a. When compared to the reference Co metal foil (Figure S10, Supporting Information), the as-synthesized sample (i.e., dry) showed higher absorption energy and a stronger white line in Co K-edge XANES spectrum confirming its oxidized Co. Rather than metallic state, it is confirmed to be nearly Co^{2+} as showing a similar XANES to that of CoO, in terms of the absorption edge position and spectral structure, which indicates the Co^{2+} coordinated with oxygen as in the prototypal MOF-74.[19] A sample immersed in 1 M KOH electrolyte without any external bias (i.e., OCP) exhibited its Co absorption edge significantly shifted to higher energy. This reveals that the cobalt in the ternary NiCoFe MOF instantly became further oxidized upon exposure to the alkaline aqueous electrolyte.

Examining XANES Co K-edge spectrum while applying an external bias (1.1 and 1.5 V vs RHE) caused further oxidation of Co while showing a gradual shift of the absorption edge to higher energy, but no dramatic change in the spectral structure of XANES (i.e., mild oxidation however the same electronic structure is maintained). The electrochemical activity of metal centers (e.g., Fe, Co, or Ni) is a function of their metal–oxygen covalency.[32,37] Increasing the oxidation state of transition metals raises their electronegativity, where d-band orbitals have fewer electrons. As a result, the overlap between d and p orbitals of the metal

© 2024 The Authors. Advanced Energy Materials published by Wiley-VCH GmbH

16146840, 0, Downloaded from https://onlinelibrary.wiley.com/doi/10.1002/aenm.202303350 by Massachusetts Institute of Technolo, Wiley Online Library on [02/04/2024]. See the Terms and Conditions (https://onlinelibrary.wiley.com/terms-and-conditions) on Wiley Online Library for rules of use; OA articles are governed by the applicable Creative Commons License

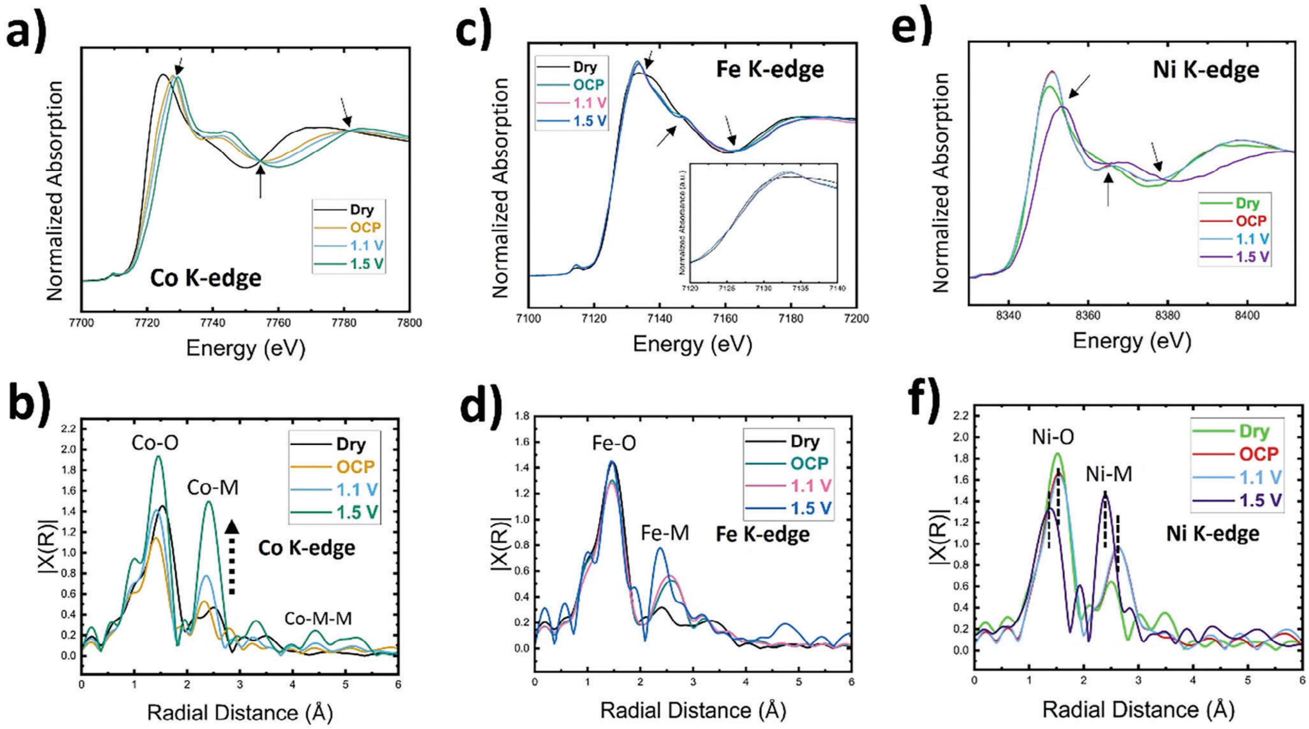

Figure 4. In situ XAS spectra of trimetallic MOF-74 tested in an air-tight 2-electrode cell with 1 м KOH electrolyte. a,b) XANES and EXAFS of Co K-edge spectra, respectively. c,d) XANES and EXAFS of Fe K-edge spectra, respectively. e,f) XANES and EXAFS of Ni K-edge spectra, respectively. In situ scans were performed under different conditions: as-synthesized (dry), OCP, pre-OER (1.1 V vs RHE), and around OER onset (1.5 V vs RHE).

catalyst and oxygen intermediates, respectively, increases. Ultimately, metal–oxygen hybridization becomes more favorable, which promotes OER activity.[30,38–42] Observed from the absorption edge positions in Figure S10 (Supporting Information), the cobalt in 1.1 and 1.5 V samples are more oxidized than Co^{2+} of $Co(OH)_2$ while being more reduced than Co_3O_4 reference. Such an observation on the oxidation state of Co, coupled with further comparison of the spectral structure of Co K-edge XANES to other reference phases, is aligned with the related literature reports suggesting that the local structures of Co in the MOF catalyst are highly similar to those in oxyhydroxide phase (CoOOH) which demonstrates a high activity towards OER.[19] The sample obtained after cutting off the external bias was probed to identify the final oxidation state of each element in the catalyst (i.e., post-mortem). Post-mortem analysis of Co K-edge XANES confirmed a slight reduction of Co from the 1.5 V sample, showing a similar absorption edge position of the 1.1 V sample. This implies that the final oxidation state of Co after OER is close to those in the CoOOH phase. In addition, this result infers that the metal centers of the designed MOF are dynamically changing their oxidation states under OER testing, corroborated by some published reports.[12,23]

The local atomistic structure of Co was revealed through extended X-ray absorption fine structure (EXAFS) analyses. Fourier-transformed EXAFS spectra for Co K-edge depicted in Figure 4b were obtained at the same conditions, as explained earlier for XANES analyses. Peaks positioned ≈1.5 and 2.4 Å are ascribed to Co—O and Co—*M* (*M* is a metal atom, Co, Ni, or Fe, as the second nearest neighboring atom), respectively. As-synthesized condition (i.e., dry) showed a very different EXAFS spectrum from other EXAFS spectra obtained in situ (i.e., OCP, 1.1, and 1.5 V counterparts), which implies a significant structural transformation taking place when the MOF-74 structure goes under OER. The first peak located at 1.542 Å of dry condition was shifted to a shorter radial distance of 1.412 Å at OCP condition, indicating ≈0.13 Å of a compressive strain.

Mechanical strain is a well-known feature that can modulate the electrocatalytic activity. Compressive strain shifts the *d*-band orbitals of the metal center of the catalyst away from the Fermi level.[43,44] In consequence, the anti-bonding states become less filled, which strengthens the interaction between OER reaction intermediates and the catalyst's metal atoms. Hence, OER electrocatalytic activity is promoted.[20,45–47] In addition to the change in bond distance, the intensity of the 2nd peak representing Co—*M* (distance between Co with its 2nd nearest neighbor) increased significantly when the dry sample was subjected to the OCP condition. This may imply the evolution of a new phase of Co under OER conditions Applying external bias to promote OER (i.e., 1.1 and 1.5 V) had a minor effect on the distances of Co—O and Co—*M* peak positions, compared to the OCP condition. This implies that MOF-74 transformation takes place under OCP, while applying external bias afterward does not contribute significantly.

Moreover, additional peaks appeared under OER conditions around 4.47 Å, which is almost double the radial distance of that of the 2nd peak for Co—*M*, when the phase shift is potentially considered. The additional peaks around 4.47 Å could be an indication of forming a Co—*M*—*M* (i.e., Co—M2 distance

© 2024 The Authors. Advanced Energy Materials published by Wiley-VCH GmbH

16146840, 0, Downloaded from https://onlinelibrary.wiley.com/doi/10.1002/aenm.202303350 by Massachusetts Institute of Technolo, Wiley Online Library on [02/04/2024]. See the Terms and Conditions (https://onlinelibrary.wiley.com/terms-and-conditions) on Wiley Online Library for rules of use; OA articles are governed by the applicable Creative Commons License

between Co and 2nd nearest metal atom) colinear arrangement (e.g., Co—Fe—Ni, or Co—Ni—Fe).[20] Presumably, the Co—*M*—*M* distance is further compressed at 1.5 V (4.425 Å). This observation agrees with other literature reports where CoOOH analogs have a shorter length for the corresponding peak than that of $Co(OH)_2$ analogs, telling that the MOF-74 catalysts evolved into the CoOOH analogs with the progression of OER.[19,20,30]

Comparing the relative intensities of Co—O/Co-*M* EXAFS peaks can reflect the change in coordination number at different stages during OER (i.e., local surroundings of the Co center). The intensity ratio of Co—O/Co—*M* peaks decreased while increasing applied bias: 2.14 to 1.3, for OCP to 1.5 V, respectively. This observation indicates a relative decrease in the oxygen presence in the vicinity of Co when compared to the content of the metal neighboring atoms corresponding to the Co-M peak. A similar phenomenon has been reported where the oxygen deficiency (i.e., the lower coordination number of O surrounding Co) is a result of forming oxygen vacancies ($V_o^{\cdot\cdot}$) at higher positive potentials in aqueous alkaline solutions.[23,48,49] Formation of oxygen vacancies has shown enhancement in the electrocatalytic activity due to improvement in electronic conductivity, in addition to the facile binding of oxygen intermediates with Co metal center.[35,50] Our ex-situ X-ray photoelectron spectroscopy (XPS) analysis shows a similar trend, where O 1s photoemissions spectrum of MOF after treatment at 1.5 V showed a significant reduction in binding energies by ≈0.5 eV, compared to O 1s spectrum of dry MOF, as shown in Figure S11 (Supporting Information). The formation of oxygen vacancies around the metal center atoms decreases the competency for the remaining oxygen atoms (more electronegative) to withdraw electrons from metal centers (less electronegative) so that the binding energy of O 1s electrons decreases.

Chemical and structural analyses of the Fe metal centers were carried out under the same test conditions. Figure 4c shows in situ XANES spectra of Fe K-edge. Results showed for the as-synthesized condition (i.e., dry) that its absorption edge was at significantly higher energies than that of FeO reference (Figure S14, Supporting Information), which indicates that the initial state of Fe in MOF was highly oxidized as expected more than Fe^{2+}. After exposing the sample to the alkaline electrolyte without applying external bias (i.e., OCP), the oxidation state of Fe further increased, as demonstrated by the XANES in which the absorption edge shifted to higher energy with the change in spectral structure. However the increase in the oxidation state of Fe was slower than that of Co. Applying an external bias to enable OER to take place (i.e., 1.1 and 1.5 V) showed a small, gradual increase in the oxidation state, as shown in the inset of Figure 4c. Fe K-edge XANES confirmed that the Fe oxidation state of the catalyst samples remained more reduced than the Fe_2O_3 reference sample, and well more oxidized than the FeO reference (Figure S12, Supporting Information), which suggests that Fe could maintain an intermediate oxidation state (e.g., $Fe(OH)_2$ and/or oxyhydroxide phase (FeOOH)), as observed in other reports.[19,20] Post-mortem XANES showed a minute reduction of Fe compared to the 1.5 V case, which agrees with the post-mortem XANES of Co K-edge. This further confirms the dynamic and irreversible transformation of the MOF structure under OER conditions. Moreover, similar to the Co K-edge XANES, a few isosbestic points were observed in Fe K-edge XANES, implying the differences in the XANES spectra are from the composition change of multiple phases induced by the progression of OER.

The structural analysis of the Fe vicinity (i.e., nearest neighbors) was performed by examining EXAFS spectra. As shown for the Co K-edge EXAFS case, a significant increase in the peak intensity representing the Fe-M peak (≈ 2.5 Å) was observed for the OCP condition when compared to the corresponding peak of the dry condition spectrum.16,48,49 Applying external bias resulted in increasing the relative intensity of Fe-*M* peak (to that of Fe-O peak) as well as shifting its position shorter radial distance (i.e., compressive strain), as shown in Figure 4d.

Ni K-edge XAS analysis was performed to unravel its chemical and structural configuration changes under different OER conditions. The as-synthesized spectrum of Ni K-edge showed a positive shift in oxidation state compared to Ni metal foil, confirming that its initial state is an oxide phase. XANES spectra in Figure 4e showed an increase of Ni valence upon immersing the sample in 1 м KOH electrolyte (i.e., OCP), which was also demonstrated by the evolution of the Ni-M peak in the EXAFS in Figure 4f. Then, no noticeable change was observed in either the XANES or EXAFS when applying external bias at 1.1 V versus RHE. Around the OER onset (i.e., at 1.5 V) significant abrupt increase in the Ni oxidation state was observed, where Ni K-edge aligned with that of Nickel oxyhydroxide (NiOOH) reported in the literature, as shown in Figure S13 (Supporting Information).[20,51] EXAFS spectra of Ni K-edge, presented in Figure 4f, showed a significant influence of OER condition on the distances of Ni—O and Ni—M peaks. Around OER onset (i.e., 1.5 V), significant compression of Ni—O and Ni—M distances was observed, by 0.17 and 0.24 Å, respectively, compared to their respective distances at 1.1 V. The significant reduction in distances aligns with the transformation of Ni moieties to form NiOOH analogs.[20,51,52] In summary, the promotion of OER catalytic activity of the tri-metallic MOFs can be ascribed to multiple factors including an increase in the metals' oxidation state, where the binding affinity of OER intermediates with catalysts' metal centers became favorable, the presence of compressive strain during OER, formation of the highly active oxyhydroxide phase, and enhancement of charge transfer due to the formation of oxygen vacancies.

2.4. Full Cell Membrane Electrode Assembly Testing

Translation of lab-scale performance into an actual device (i.e., the single-cell device of anode/membrane/cathode assembly) has been a great challenge in the electrolysis field, among which is AEMEC. The current density at which the single cell of a water electrolyzer operates is strongly related to the amount of hydrogen generated, but also affects the lifetime of the MEA components (especially the catalyst). The voltage at which the cell operates is another important factor that determines the total energy consumption needed to produce green hydrogen. Ultimately, higher current density, at a low voltage (i.e., small overpotential), operating for several hundreds of hours, is deemed as the first step to success to enable AEMEC to penetrate the market and daily life applications.

Different synthesized MOFs with modified chemistries have been tested in a single-cell AEMEC, to unravel their device-level performance. Tests were performed where MOFs were used as

© 2024 The Authors. Advanced Energy Materials published by Wiley-VCH GmbH

16146840, 0, Downloaded from https://onlinelibrary.wiley.com/doi/10.1002/aenm.202303350 by Massachusetts Institute of Technolo, Wiley Online Library on [02/04/2024]. See the Terms and Conditions (https://onlinelibrary.wiley.com/terms-and-conditions) on Wiley Online Library for rules of use; OA articles are governed by the applicable Creative Commons License

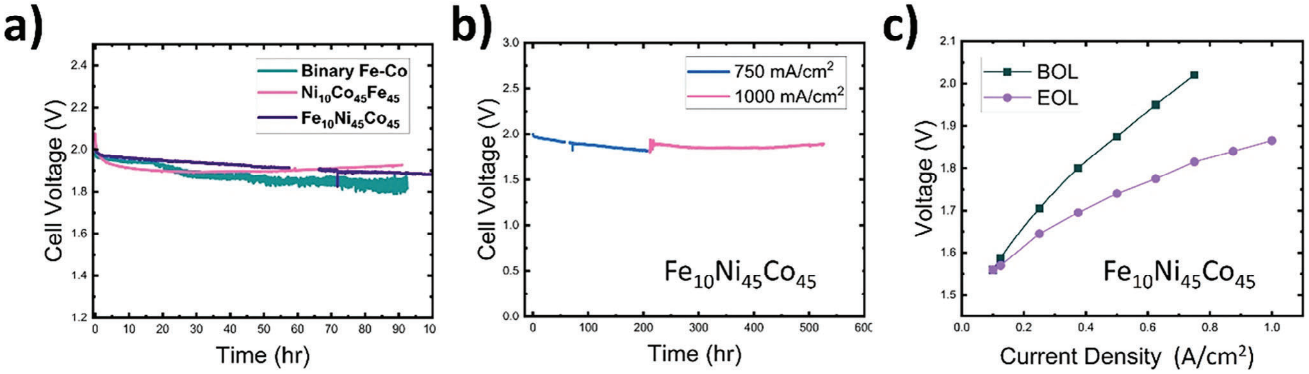

Figure 5. a) Cell voltage versus time for MEAs with three catalysts at 0.75 A cm^{-2}. b) Cell voltage versus time for ternary $Fe_{10}Co_{45}Ni_{45}$ MOF at 0.75 A cm^{-2} and 1 A cm^{-2}. c) Steady-state polarization curves at the beginning of life (BOL) and end of life (EOL) for the cell tested in (b).

OER catalysts at the anode side, while commercial Pt/carbon was used as a hydrogen evolution (HER) catalyst at the cathode side. At the anode side, 0.1 M sodium hydroxide (NaOH) solution was flowed as an electrolyte, while the cell temperature was kept at 60 °C for the entire testing period, as shown in **Figure** 5a. Binary Fe-Co MOF was tested as an OER catalyst in the MEA setup of a full-cell testing mode. Results showed that to maintain a current density of 750 mA cm^{-2}, AEMEC full cell voltage was initially at 2 V. After a few hours, MEA showed initial signs of MEA activation, where the voltage slightly dropped to remain ≈1.95–1.85 V afterward. MEAs require a break-in period which entails completing the ion exchange and hydrating processes. Samples maintained a very good performance for 90 h, before the cell voltage increased. Increasing the cell voltage is an indication of initial signs of MEA degradation. Several factors could contribute to cell degradation (e.g., catalyst degradation, catalyst layer delamination due to weakened bonding with the electrode, and ionomer/binder degradation, among others). All the MEAs in the presented study were fabricated identically, while the only difference is the OER catalyst. Thus, MEA degradation can be attributed primarily to the catalyst material. Ternary $Ni_{10}Co_{45}Fe_{45}$ catalyst was then tested in an identical MEA full-cell setup. Results showed a slightly higher cell voltage of 2.09 V at the kickoff of testing. Afterward, cell voltage dropped significantly to 1.9 V within the first 10 h of testing. Shortly after, cell voltage kept increasing to reach 1.95 V at the 50 h mark. This indicates that cell degradation started to take place.

It is worth mentioning that the increase in the voltage profile during chronoamperometry tests carried out in 3-electrode cells, was not observed during MEA testing. In a 3-electrode setup and at elevated current densities, gas bubbles from the electrolyte form at the interface between the catalyst surface and electrolyte. Gas bubbles accumulate with time and lead to a reduction in the electrochemically active surface area (ECSA). That leads to a gradual increase in the overpotential (i.e., the recorded potential value increases too). To release the accumulation of gas bubbles, it is recommended to cut off the applied current and hold the sample at open circuit condition for a short period (≈30 min), every 5–10 h intervals of chronoamperometry.[12,13,53] On the contrary, in the MEA setup, the electrolyte is continuously circulated through a pump which could help release the gas bubbles formation off the catalyst surface. Moreover, during testing in a 3-electrode electrochemical setup, the catalysts were supported on carbon fiber paper. Carbon fiber paper could be corroded at elevated current densities and pH 14, according to the Pourbaix diagram. Carbon corrosion could result in reducing the active ECSA, in addition to contaminating the electrolyte, which results in increasing the potential during chronoamperometry measurements. On the contrary, MEA testing was done where the catalysts were supported on Ni-foam which is more stable than the carbon fiber paper support used throughout the testing in a 3-electrode setup. Furthermore, it is known that the long-term durability of the electrolysis cells may be impacted by other components, such as the mechanical adhesion of the catalysts to the electrode structure. The ratio of catalyst to ionomer and binder components, and the catalyst coating technique in the full cell MEA setup is different than those of preparing electrodes for 3-electrode electrochemical testing.

Ternary $Fe_{10}Co_{45}Ni_{45}$ MOF-74 was further explored with MEA full-cell. Cell performance was much superior to the other electrodes we have tried. The initial cell voltage was 2 V, which steadily went down to 1.9 V at the first 100th h. This observation implies that ternary $Fe_{10}Co_{45}Ni_{45}$ MOF is showing an extremely stable performance. Cell voltage trend remained the same (i.e., decreasing with time), while at the 200-h mark of testing, the cell voltage reached 1.8 V. Hence, the current density of the cell was significantly increased from 750 mA cm^{-2} to reach an elevated level of 1000 mA cm^{-2}, which is desirable for industrial applications (as H_2 generation scales with cell current). It is worth noting that the current density of 1000 mA cm^{-2} is very harsh, where typical cells may fail within several tens of hours. MEA of ternary $Fe_{10}Co_{45}Ni_{45}$ MOF had a slight jump in potential from 1.8 V to reaching 1.9 V (≈5%) upon current density increase by 33%. Cell voltage remained very stable at 1000 mA cm^{-2} between 1.9 and 1.95 V, up to 550 h of testing, as shown in Figure 5b. This is believed to be a tremendously efficient and stable performance, among those presented in the literature. The cell experienced slow degradation for an additional 100 h with a decay rate of 0.4 μV h^{-1}. Figure 5c shows the steady state polarization curves for the MEA fabricated by ternary $Fe_{10}Co_{45}Ni_{45}$ MOF catalyst. It is worth noting that the steady-state polarization curves relate more to the real application, where the concentration profiles are well established under a certain current density. Compared with the beginning-of-life (BOL) performance (0.37 A cm^{-2} @ 1.8 V), the

© 2024 The Authors. Advanced Energy Materials published by Wiley-VCH GmbH

16146840, 0, Downloaded from https://onlinelibrary.wiley.com/doi/10.1002/aenm.202303350 by Massachusetts Institute of Technolo, Wiley Online Library on [02/04/2024]. See the Terms and Conditions (https://onlinelibrary.wiley.com/terms-and-conditions) on Wiley Online Library for rules of use; OA articles are governed by the applicable Creative Commons License

current density at 1.8 V increased to 0.72 A cm^{-2} at the end-of-life (EOL), almost a 100% increase, as shown in Figure 5c. To the best of our knowledge, the durability of AEM electrolysis has been a challenge for non-noble metal catalysts, and our MOF catalysts reported herein show an excellent balance between high electrochemical activity and high stability, representing one of the best non-noble metal catalysts to date in the literature.

The break-in process is known to help improve the performance during the very few 10s of hours of testing. It is also worth mentioning that many catalysts go through chemical and structural evolution under OER conditions, as widely shown in the literature.[9–13] Some reports showed a continuous performance enhancement during testing for thousands of cycles.[9,14] Our MOF catalysts have shown a tendency to go through chemical and structural evolution, as revealed through the in situ XAS analysis section (Figure 4). It could be quite reasonable, based on other literature, that our MOF catalyst can go through continuous chemical and structural changes which lead to an increase in performance enhancement with testing. For example, MOFs are multi-channel porous systems. Some of those channels could be blocked or not have access to reactants at the early stage of testing. While testing evolves, more channels become open which leads to an increase in ECSA, which in return will lead to an increase in performance. Furthermore, SEM imaging (Figure S17, Supporting Information) showed that the as-synthesized MOF particles are highly stacked together to form clusters. During MEA preparation, MOF powders are ground and then sonicated, however, this may not be very efficient to fully separate the particles from one another. The separation may happen under OER conditions where electrolyte pumping and continuous oxygen bubbles evolution may induce capillary forces which help to unstack the particles and increase the ECSA, as well.

The presented thesis herein provides the most comprehensive exploration of tri-metallic MOFs, encompassing diverse chemical compositions of Fe, Ni, and Co. Twenty-five distinct isostructural MOFs were meticulously examined in the presented study, delving into the individual contributions of each of the three metals to the OER activity. This systematic investigation provides valuable insights into the interplay between these elements and their impact on catalytic performance. Ultimately, we succeeded in identifying an analog ($Fe_{10}Ni_{45}Co_{45}$) that marks an outstanding OER performance in an actual AEMEC device at harsh conditions (industrial scale current density 1 A cm^{-2}). Our study provides an important technological advancement toward enabling the production of green hydrogen at a higher Technology Readiness Level (TRL) at a significantly lower cost compared to noble metal catalysts.

3. Conclusion

Non-precious trimetallic electrocatalysts have been synthesized based on the MOF-74 structure. Tuning the metal cation compositions affected the electrocatalytic performance toward alkaline aqueous OER. The optimal composition has been found where Ni and Co contents are similarly rich, while Fe content is lean. The structure of MOF-74 goes through abrupt structural and chemical transformations under OER. Our samples obtained the highly active oxyhydroxide moieties for Co, Fe, and Ni. Mechanical strain was induced on the interatomic distance of the metal center with nearest neighbors, which promoted OER activity. In addition, metal centers experienced an increase in their oxidation state under OER conditions, where the metal-oxygen covalency becomes stronger, which further facilitates OER. During OER, a tendency to form oxygen vacancies in the vicinity of Co was observed, which leads to better electronic conductivity and faster charge transfer kinetics. Our developed MOF-74 has been used as the anode catalyst for OER in a full-cell anion exchange membrane electrolyzer. Catalysts showed great stability at higher current densities of 750 and 1000 mA cm^{-2} for 550 h without noticeable decay in the performance. This is very encouraging for green hydrogen production, CO_2 reduction, etc.

Supporting Information

Supporting Information is available from the Wiley Online Library or from the author.

Acknowledgements

The authors acknowledge the European Synchrotron Radiation Facility (ESRF) for the provision of synchrotron radiation facilities and would like to thank Dr. Viktoriia Saveleva and Dr. Pieter Glatzel for assistance and support in using beamline ID26 during the experimental session MA5352 (https://doi.org/10.15151/ESRF-ES-744180074). In addition, this research used resources of the Advanced Photon Source (APS), an Office of Science User Facility operated for the U.S. Department of Energy (DOE) Office of Science by Argonne National Laboratory and was supported by the U.S. DOE under Contract No. DE-AC02-06CH11357, and the Canadian Light Source and its funding partners. The authors thank Dr. Tianpin Wu and Dr. George Sterbinsky from 9BM beamline, and Dr. Debora Motta Meira and Dr. Zou Finfrock from 20BM beamline for assistance in collecting the XAS data.

Conflict of Interest

The authors declare no conflict of interest.

Data Availability Statement

The data that support the findings of this study are available from the corresponding author upon reasonable request.

Keywords

electrolyzer full cell, in situ characterization, metal–organic frameworks, multi-metal catalyst, oxygen evolution reaction, water electrolysis

Received: October 5, 2023
Revised: February 13, 2024
Published online:

[1] Y. Huang, J. Li, Y. Huang, J. Li, *Adv. Energy Mater.* **2022**, *12*, 2202197.
[2] Y. Zheng, Y. Jiao, M. Jaroniec, S. Z. Qiao, *Angew. Chem. Int. Ed.* **2015**, *54*, 52.
[3] T. N. Veziroglu, *Energy Procedia* **2012**, *29*, 654.

© 2024 The Authors. Advanced Energy Materials published by Wiley-VCH GmbH

16146840, 0, Downloaded from https://onlinelibrary.wiley.com/doi/10.1002/aenm.202303350 by Massachusetts Institute of Technolo, Wiley Online Library on [02/04/2024]. See the Terms and Conditions (https://onlinelibrary.wiley.com/terms-and-conditions) on Wiley Online Library for rules of use; OA articles are governed by the applicable Creative Commons License

[4] A. A. Abdelhafiz, M. A. Ganzoury, A. W. Amer, A. A. Faiad, A. M. Khalifa, S. Y. Alqaradawi, M. A. El-Sayed, F. M. Alamgir, N. K. Allam, *Phys. Chem. Chem. Phys.* **2018**, *20*, 10258.
[5] K. E. Salem, A. M. Mokhtar, A. Abdelhafiz, N. K. Allam, *ACS Appl. Nano Mater.* **2020**, *3*, 6078.
[6] X. Xie, L. Du, L. Yan, S. Park, Y. Qiu, J. Sokolowski, W. Wang, Y. Shao, *Adv. Funct. Mater.* **2022**, *32*, 2110036.
[7] M. Bernt, A. Hartig-Weiß, M. F. Tovini, H. A. El-Sayed, C. Schramm, J. Schröter, C. Gebauer, H. A. Gasteiger, *Chem. Ing. Tech.* **2020**, *92*, 31.
[8] N. Ul Hassan, M. Mandal, G. Huang, H. A. Firouzjaie, P. A. Kohl, W. E. Mustain, *Adv. Energy Mater.* **2020**, *10*, 2001986.
[9] W. E. Mustain, P. A. Kohl, *Nat Energy* **2020**, *5*, 359.
[10] N. Du, C. Roy, R. Peach, M. Turnbull, S. Thiele, C. Bock, *Chem. Rev.* **2021**, *122*, 11830.
[11] J. R. Varcoe, P. Atanassov, D. R. Dekel, A. M. Herring, M. A. Hickner, P. A. Kohl, A. R. Kucernak, W. E. Mustain, K. Nijmeijer, K. Scott, T. Xu, L. Zhuang, *Energy Environ. Sci.* **2014**, *7*, 3135.
[12] A. Abdelhafiz, B. Wang, A. R. Harutyunyan, J. Li, *Adv. Energy Mater.* **2022**, *12*, 2200742.
[13] A. Abdelhafiz, A. N. M. Tanvir, M. Zeng, B. Wang, Z. Ren, A. R. Harutyunyan, Y. Zhang, J. Li, *Adv. Sci.* **2023**, *10*, 2300426.
[14] Z. Hao, P. Wei, H. Kang, Y. Yang, J. Li, X. Chen, D. Guo, L. Liu, *Nanotechnology* **2020**, *31*, 435707.
[15] K. E. Salem, A. A. Saleh, G. E. Khedr, B. S. Shaheen, N. K. Allam, *Energy Environ. Mater.* **2023**, *6*, e12324.
[16] Z. Wan, D. Yang, J. Chen, J. Tian, T. T. Isimjan, X. Yang, *ACS Appl. Nano Mater.* **2019**, *2*, 6334.
[17] Z. Ji, T. Li, O. M. Yaghi, *Science* **2020**, *369*, 674.
[18] S. Deng, Z. Li, K. Xu, Z. Liu, Z. Yin, H. Yu, J. Lv, L. Yang, Z. Sun, M. Zhang, *J. Electrochem. Soc.* **2021**, *168*, 082504.
[19] L. Bai, C. S. Hsu, D. T. L. Alexander, H. M. Chen, X. Hu, *J. Am. Chem. Soc.* **2019**, *141*, 14190.
[20] W. Cheng, X. Zhao, H. Su, F. Tang, W. Che, H. Zhang, Q. Liu, *Nat. Energy* **2019**, *4*, 115.
[21] Q. Shi, S. Fu, C. Zhu, J. Song, D. Du, Y. Lin, *Mater. Horiz.* **2019**, *6*, 684.
[22] S. Li, Y. Gao, N. Li, L. Ge, X. Bu, P. Feng, *Energy Environ. Sci.* **2021**, *14*, 1897.
[23] S. Zhao, C. Tan, C. T. He, P. An, F. Xie, S. Jiang, Y. Zhu, K. H. Wu, B. Zhang, H. Li, J. Zhang, Y. Chen, S. Liu, J. Dong, Z. Tang, *Nat. Energy* **2020**, *5*, 881.
[24] L. J. Wang, H. Deng, H. Furukawa, F. Gándara, K. E. Cordova, D. Peri, O. M. Yaghi, *Inorg. Chem.* **2014**, *53*, 5881.
[25] S. R. Caskey, A. G. Wong-Foy, A. J. Matzger, *J. Am. Chem. Soc.* **2008**, *130*, 10870.
[26] N. L. Rosi, J. Kim, M. Eddaoudi, B. Chen, M. O'Keeffe, O. M. Yaghi, *J. Am. Chem. Soc.* **2005**, *127*, 1504.
[27] J. Joseph, S. Iftekhar, V. Srivastava, Z. Fallah, E. N. Zare, M. Sillanpää, *Chemosphere* **2021**, *284*, 131171.
[28] S. Zhang, Y. Zhang, F. Baig, T. F. Liu, *Cryst. Growth Des.* **2021**, *21*, 3100.
[29] Z. Chen, J. Wang, D. Chao, T. Baikie, L. Bai, S. Chen, Y. Zhao, T. Chien Sum, J. Lin, Z. Shen, *Sci. Rep.* **2016**, *6*, 25771.
[30] K. Cysewska, M. Zając, M. Łapiński, J. Karczewski, M. K. Rybarczyk, B. Kamecki, P. Jasiński, S. Molin, *Energy Technol.* **2021**, *9*, 2100688.
[31] Z. Xiao, Y. Jiang, H. Wu, H. Zhong, H. Song, A. Abdelhafiz, J. Zeng, *J. Alloys Compd.* **2021**, *877*, 160221.
[32] N. Li, R. G. Hadt, D. Hayes, L. X. Chen, D. G. Nocera, *Nat. Commun.* **2021**, *12*, https://doi.org/10.1038/s41467-021-24453-6.
[33] Y. Dou, C. T. He, L. Zhang, M. Al-Mamun, H. Guo, W. Zhang, Q. Xia, J. Xu, L. Jiang, Y. Wang, P. Liu, X. M. Chen, H. Yin, H. Zhao, *Cell. Rep. Phys. Sci.* **2020**, *1*, 100077.
[34] A. Grimaud, O. Diaz-Morales, B. Han, W. T. Hong, Y. L. Lee, L. Giordano, K. A. Stoerzinger, M. T. M. Koper, Y. Shao-Horn, *Nat. Chem.* **2017**, *9*, 457.
[35] Y. Zhu, L. Zhang, B. Zhao, H. Chen, X. Liu, R. Zhao, X. Wang, J. Liu, Y. Chen, M. Liu, Y. M. Zhu, H. J. Chen, X. Liu, J. Liu, Y. Chen, L. Zhang, B. T. Zhao, M. L. Liu, R. Zhao, X. W. Wang, *Adv. Funct. Mater.* **2019**, *29*, 1901783.
[36] D. Zhen, B. Zhao, H.-C. Shin, Y. Bu, Y. Ding, G. He, M. Liu, D. X. Zhen, B. T. Zhao, Y. F. Bu, Y. Ding, M. L. Liu, G. He, H. Shin, *Adv. Mater. Interfaces* **2017**, *4*, 1700146.
[37] W. Li, W. Fang, C. Wu, K. N. Dinh, H. Ren, L. Zhao, C. Liu, Q. Yan, *J. Mater. Chem. A Mater.* **2020**, *8*, 3658.
[38] S. Yeo, A. T. Bell, *J. Am. Chem. Soc.* **2011**, *133*, 5587.
[39] N. H. Chou, P. N. Ross, A. T. Bell, T. D. Tilley, *ChemSusChem* **2011**, *4*, 1566.
[40] Y. Zhu, W. Zhou, J. Yu, Y. Chen, M. Liu, Z. Shao, *Chem. Mater.* **2016**, *28*, 1691.
[41] Y. Zhu, W. Zhou, Y. Zhong, Y. Bu, X. Chen, Q. Zhong, M. Liu, Z. Shao, *Adv. Energy Mater.* **2017**, *17*, 1602122.
[42] Y. Zhu, W. Zhou, J. Sunarso, Y. Zhong, Z. Shao, *Adv. Funct. Mater.* **2016**, *26*, 5862.
[43] A. Abdelhafiz, A. Vitale, C. Joiner, E. Vogel, F. M. Alamgir, *ACS Appl. Mater. Interfaces* **2015**, *7*, 6180.
[44] A. Abdelhafiz, A. Vitale, P. Buntin, B. deGlee, C. Joiner, A. Robertson, E. M. Vogel, J. Warner, F. M. Alamgir, *Energy Environ. Sci.* **2018**, *11*, 1610.
[45] L. Wang, K. A. Stoerzinger, L. Chang, X. Yin, Y. Li, C. S. Tang, E. Jia, M. E. Bowden, Z. Yang, A. Abdelsamie, L. You, R. Guo, J. Chen, A. Rusydi, J. Wang, S. A. Chambers, Y. Du, *ACS Appl. Mater. Interfaces* **2019**, *11*, 12941.
[46] X. Yang, Y. Wang, X. Tong, N. Yang, X. Yang, Y. Wang, X. Tong, N. Yang, *Adv. Energy Mater.* **2022**, *12*, 2102261.
[47] W. Sun, Z. Wang, W. Q. Zaman, Z. Zhou, L. Cao, X. Q. Gong, J. Yang, *Chem. Commun.* **2018**, *54*, 996.
[48] M. Wuttig, D. Lüsebrink, D. Wamwangi, W. Wełnic, M. Gilleen, R. Dronskowski, *Nat. Mater.* **2006**, *6*, 122.
[49] D. Drevon, M. Görlin, P. Chernev, L. Xi, H. Dau, K. M. Lange, *Sci. Rep.* **2019**, *9*, 1532.
[50] B. Zhao, L. Zhang, D. Zhen, S. Yoo, Y. Ding, D. Chen, Y. Chen, Q. Zhang, B. Doyle, X. Xiong, M. Liu, *Nat. Commun.* **2017**, https://doi.org/10.1038/ncomms14586.
[51] F. Song, M. M. Busch, B. Lassalle-Kaiser, C. S. Hsu, E. Petkucheva, M. Bensimon, H. M. Chen, C. Corminboeuf, X. Hu, *ACS Cent. Sci.* **2019**, *5*, 558.
[52] M. Gorlin, J. F. De Araujo, H. Schmies, D. Bernsmeier, S. Dresp, M. Gliech, Z. Jusys, P. Chernev, R. Kraehnert, H. Dau, P. Strasser, *J. Am. Chem. Soc.* **2017**, *139*, 2070.
[53] J. Abed, S. Ahmadi, L. Laverdure, A. Abdellah, C. P. O'Brien, K. Cole, P. Sobrinho, D. Sinton, D. Higgins, N. J. Mosey, S. J. Thorpe, E. H. Sargent, *Adv. Mater.* **2021**, *33*, 2103812.

© 2024 The Authors. Advanced Energy Materials published by Wiley-VCH GmbH

16146840, 0, Downloaded from https://onlinelibrary.wiley.com/doi/10.1002/aenm.202303350 by Massachusetts Institute of Technolo, Wiley Online Library on [02/04/2024]. See the Terms and Conditions (https://onlinelibrary.wiley.com/terms-and-conditions) on Wiley Online Library for rules of use; OA articles are governed by the applicable Creative Commons License

ADVANCED ENERGY MATERIALS

Supporting Information

for *Adv. Energy Mater.*, DOI 10.1002/aenm.202303350

Tri-Metallic Catalyst for Oxygen Evolution Reaction Enables Continuous Operation of Anion Exchange Membrane Electrolyzer at 1A cm^{-2} for Hundreds of Hours

Ali Abdelhafiz, Mona H. Mohammed, Jehad Abed, Dong-Chan Lee, Mengjie Chen, Ahmed S. Helal, Zhichu Ren, Faisal Alamgir, Edward Sargent, Paul A. Kohl, Sameh K. Elsaidi* and Ju Li**

Tri-metallic Catalyst for Oxygen Evolution Reaction Enables Continuous Operation of Anion Exchange Membrane Electrolyzer at 1 A/cm^2

Ali Abdelhafiz[1,]*, Mona H. Mohammed[2,3], Jehad Abed[4], Dong-Chan Lee[5,6], Mengjie Chen[7], Ahmed S. Helal[8,9,10], Zhichu Ren[10], Faisal Alamgir[5], Edward Sargent[11], Paul A. Kohl[7], Sameh K. Elsaidi[2,3]*, Ju Li[1,10,]*

[1] Department of Nuclear Science and Engineering, Massachusetts Institute of Technology, 77 Massachusetts Ave, Cambridge, MA 02139, USA
[2] Department of Chemistry, Illinois Institute of Technology, Chicago, IL, 60616, USA
[3] SE-MAT Smartly Engineered Materials LLC, Pittsburgh, PA 15238, USA
[4] Department of Materials Science and Engineering, University of Toronto, Toronto, Ontario M5S 3G4, Canada
[5] School of Materials Science and Engineering, Georgia Institute of Technology, 771 Ferst Dr NW, Atlanta, GA, 30332, USA
[6] Department of Chemical Engineering, Hongik University, 94 Wausan-ro Mapo-gu, Seoul, 04066, Republic of Korea
[7] School of Chemical and Biomolecular and Engineering, Georgia Institute of Technology, 311 Ferst Dr NW, Atlanta, GA, 30332, USA
[8] Department of Nano Engineering, Faculty of Nanotechnology for Postgraduate Studies, Sheikh Zayed Branch Campus, Cairo University, Sheikh Zayed City 12588, Egypt
[9] Nanotechnology and Advanced Materials Laboratory, Nuclear Materials Authority, 3rd settlement 11936, Egypt
[10] Department of Materials Science and Engineering, Massachusetts Institute of Technology, 77 Massachusetts Ave, Cambridge, MA 02139, USA
[11] Department of Chemistry, Northwestern University, 2145 Sheridan Road, Evanston, IL 60208, USA

Corresponding author email: liju@mit.edu

Materials:

All chemicals have been purchased from Sigma Aldrich. All solvents including dimethyl formamide, ethanol, and methanol were purchased from Fisher Scientific. All chemicals and solvents were used as received without further purification. The 2,5-dihydroxyterephthalic acid has been purchased from Sigma Aldrich. We tried other companies, but the ligand color was greenish yellow which is different from the yellow color of the ligand from Sigma Aldrich and negatively impacted the material's performance.

Synthesis:

In a Teflon autoclave, the three metal salts are mixed in different ratios (see Table S1) with 0.05 g dobdc ligand (approximately 3:2 total metals:Ligand) in a solvent mixture of 15:1:1 dimethyl formamide (DMF), water, and ethanol. The mixtures were then kept at 130 °C for 2 days. After cooling, the materials were washed with DMF and then ethanol to remove any unreacted species. The samples were then exchanged with methanol for three days (2 times/day). The powder materials were then collected using vacuum filtration. The materials were activated using a Micromeritics Smart VacPrep station at 150 °C for 12 hours. The scaling up of the samples has been performed by multiplying the concentrations of metals and ligand and amounts of solvents by a factor.

Table S1: MOF chemical composition and precursors loadings percentages

MOF	$Ni(NO_3)_2·6H_2O$ (g)	$Co(NO_3)_2·6H_2O$ (g)	$FeSO_4·7H_2O$ (g)
$Ni_{50}Co_{50}$	0.05	0.05	0
$Ni_{50}Fe_{50}$	0.05	0	0.05
$Co_{50}Fe_{50}$	0	0.05	0.05
$Co_{80}Fe_{20}$	0	0.08	0.02
$Ni_5Co_{47.5}Fe_{47.5}$	0.005	0.0475	0.0475
$Ni_{10}Co_{45}Fe_{45}$	0.01	0.045	0.045
$Ni_{33}Co_{33}Fe_{33}$	0.033	0.033	0.033
$Ni_{50}Co_{25}Fe_{25}$	0.050	0.025	0.025
$Ni_{80}Co_{10}Fe_{10}$	0.08	0.01	0.01
$Fe_{10}Ni_{45}Co_{45}$	0.045	0.045	0.01
$Fe_{20}Ni_{40}Co_{40}$	0.04	0.04	0.02
$Fe_{50}Ni_{25}Co_{25}$	0.025	0.025	0.05
$Fe_{80}Ni_{10}Co_{10}$	0.01	0.01	0.08
$Co_{10}Ni_{45}Fe_{45}$	0.045	0.01	0.045
$Co_{50}Ni_{25}Fe_{25}$	0.025	0.05	0.025
$Co_{90}Ni_5Fe_5$	0.005	0.09	0.005

Characterization methods

Powder X-ray Diffraction (PXRD Analyses.

Powder X-ray diffraction (PXRD) patterns were collected on an STOE-STADI powder diffractometer operating at 40 kV voltage and 40 mA current with Cu-Kα1 X-ray radiation (λ = 0.154056 nm) in transmission geometry.

Surface area measurements.

N_2 sorption isotherms were collected on a Micromeritics 3Flex gas adsorption and surface area analyzer. Approximately 50-150 mg of each sample was added into a pre-weighed sample analysis tube. The samples were activated using Smart VacPrep 067 station with Hi-Vacuum pump. A liquid N_2 bath was used to maintain the sample temperature at 77K.

MEA Fabrication

Electrode catalysts materials were sprayed on porous transport layer (PTL) using airbrush gun with N_2 gas flow. Catalyst material was first ground to refine the particles' size and deagglomerate any stacking. Solution inks were fed to the airbrush and sprayed on PTL at room temperature, followed by heating the electrode for 20 seconds to evaporate the ink solvent. Anode catalyst and PTL are MOF catalyst (without addition of any carbon black) and Ni foam. Cathode catalyst is commercial Pt-Ni catalyst deposited on non-wetproofing carbon fiber paper. Both anode and cathode electrode contain 0.7 and 1.2 mg/cm^2 catalyst loading, respectively.

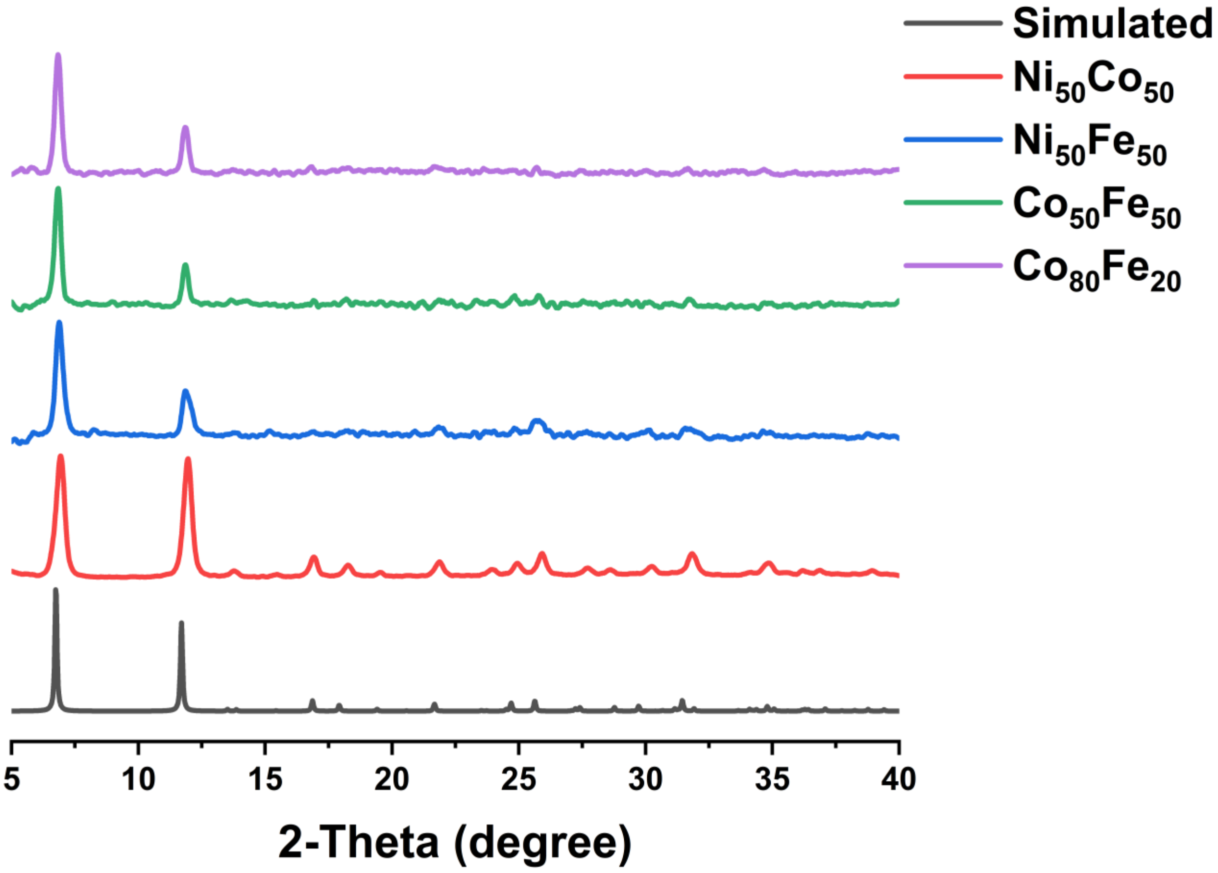

Figure S1. PXRD patterns of bimetallic MOF-74 materials compared to the simulated pattern.

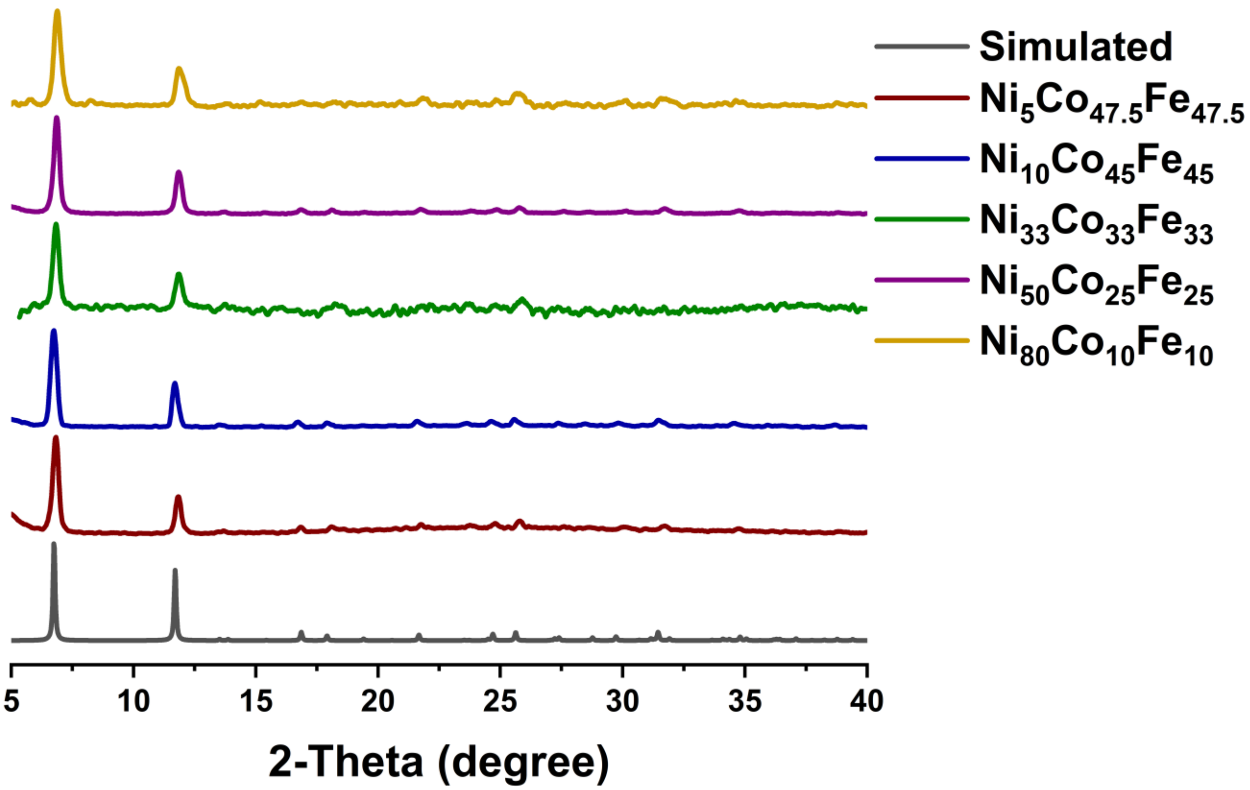

Figure S2. PXRD patterns of trimetallic MOF-74 materials of the formula ($Ni_{100-2x}Co_xFe_x$) compared to the simulated pattern.

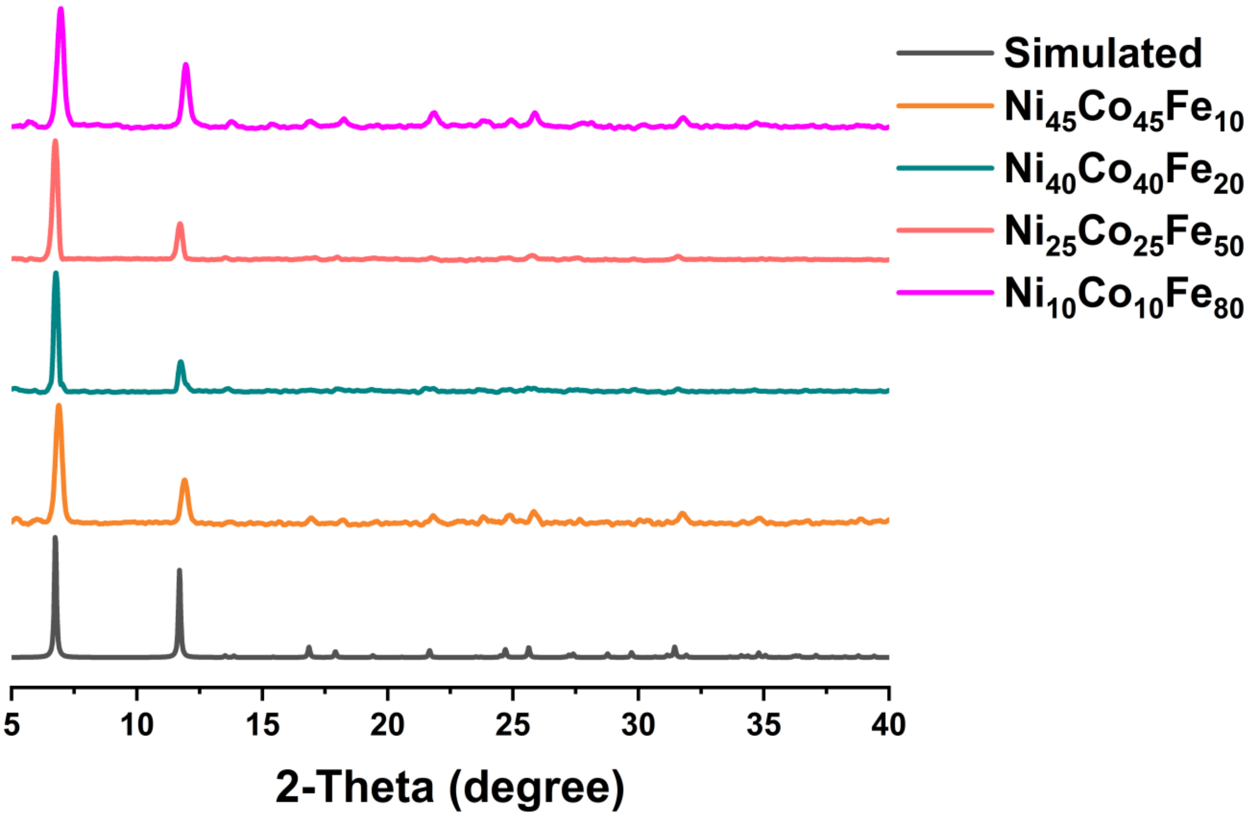

Figure S3. PXRD patterns of trimetallic MOF-74 materials of the formula ($Fe_{100-2x}Co_xNi_x$) compared to the simulated pattern.

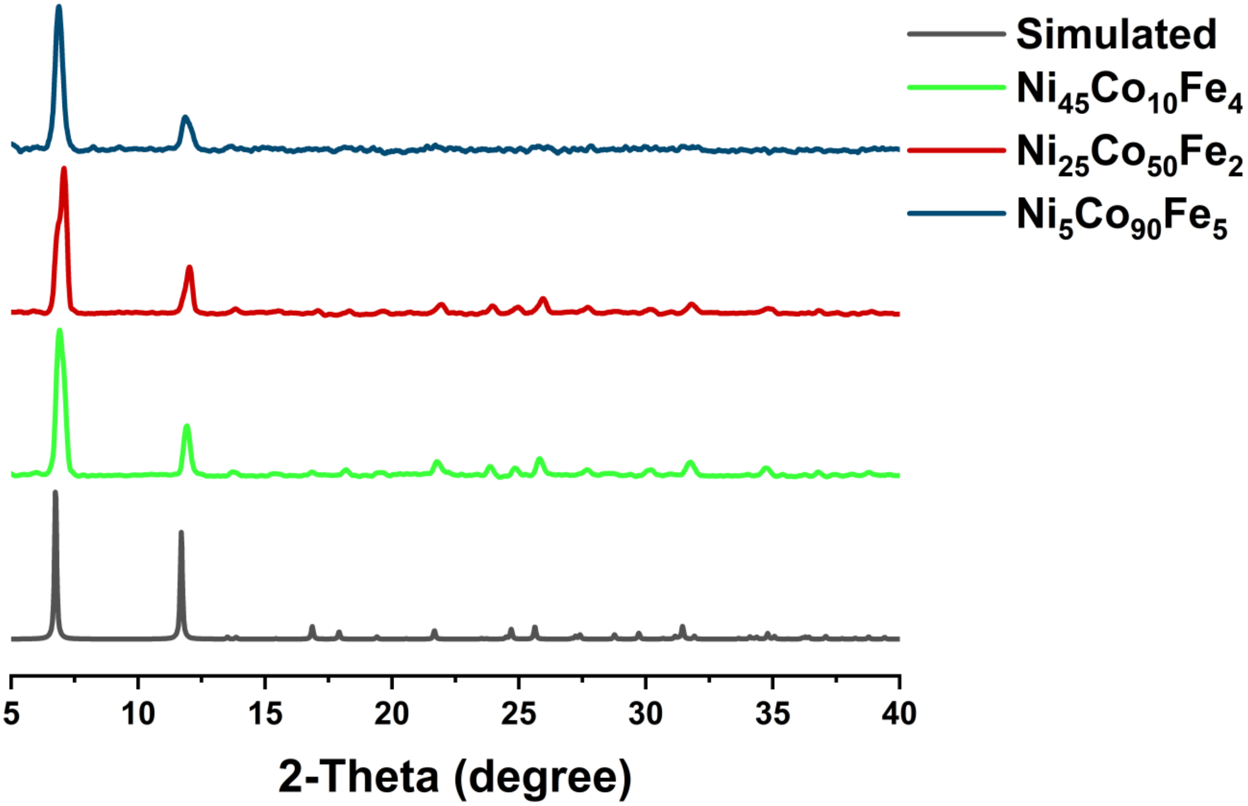

Figure S4: PXRD patterns of tri-metallic MOF-74 materials of the formula ($Co_{100-2x}Ni_xFe_x$) compared to the simulated pattern.

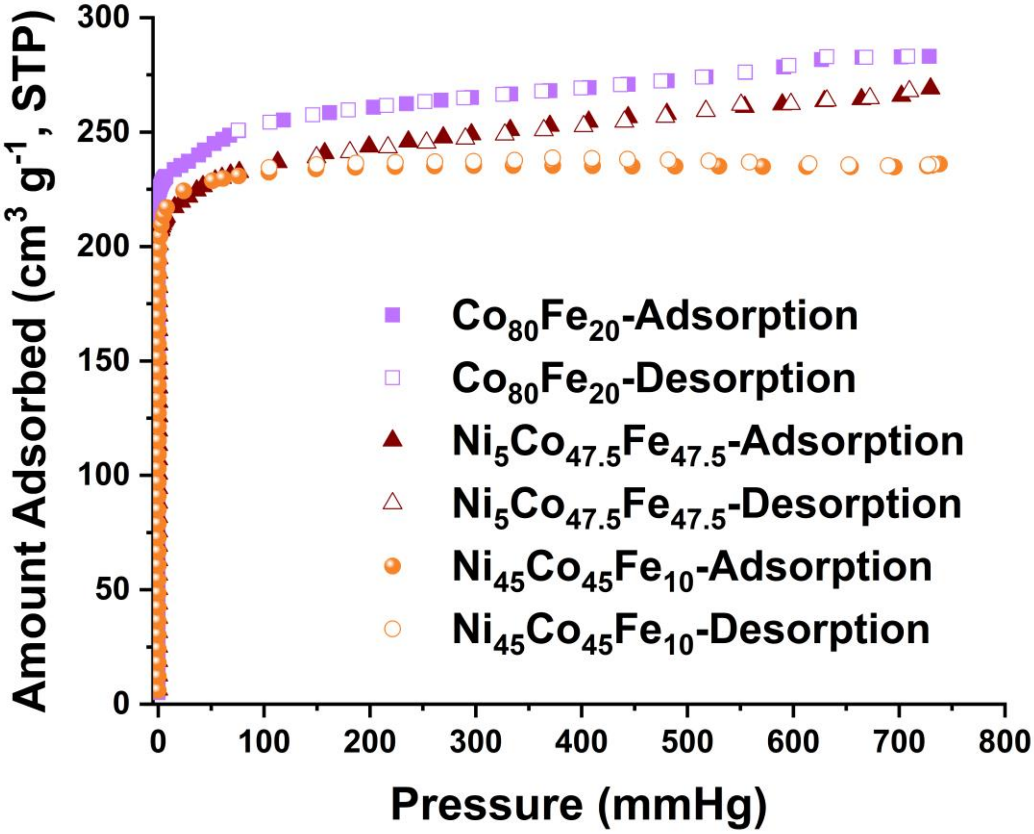

Figure S5: N_2 sorption isotherms collected at 77 °K for the activated samples.

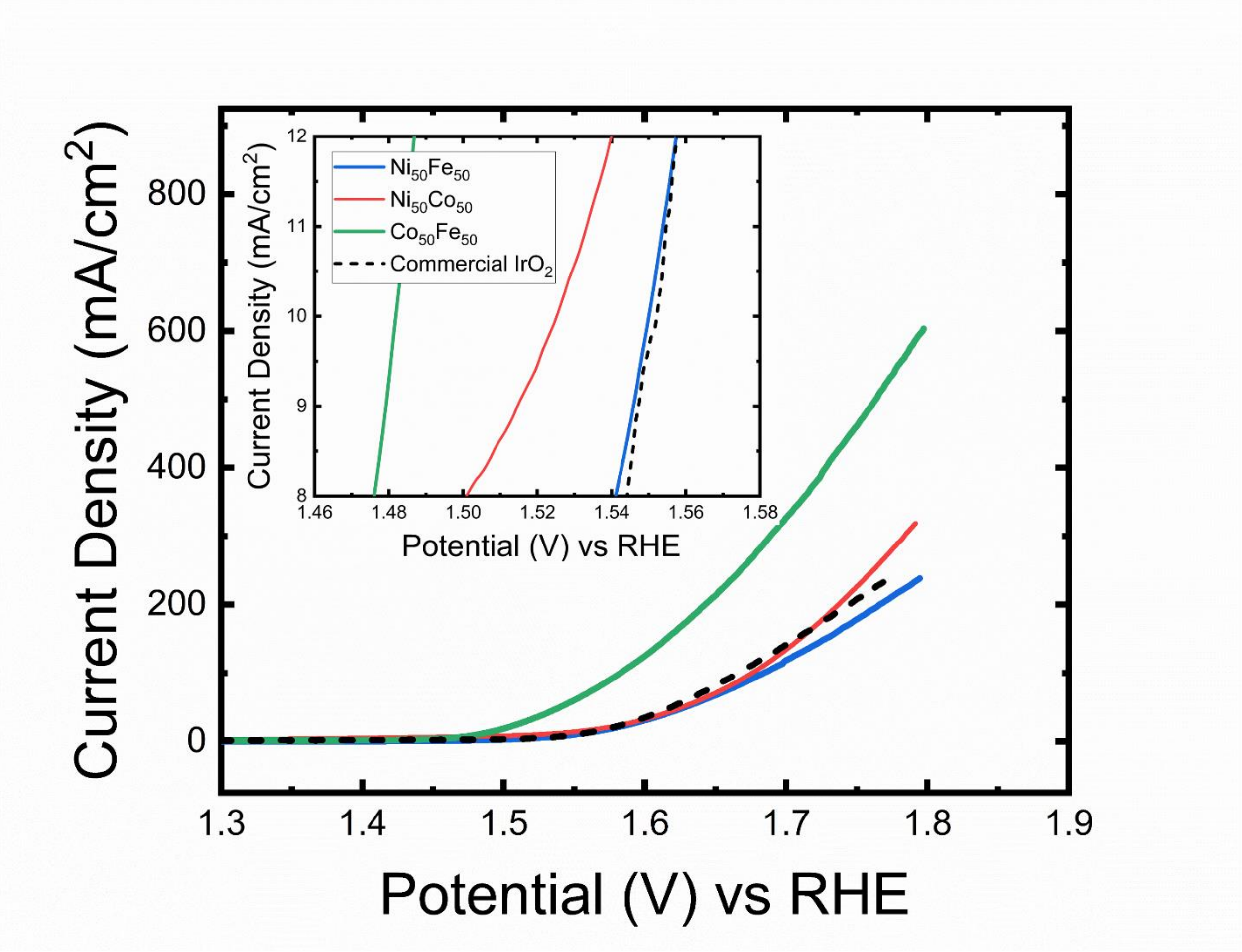

Figure S6: LSV of binary MOFs compared to commercial IrO_2 catalyst. Inset showing the performance at 10 mA/cm^2.

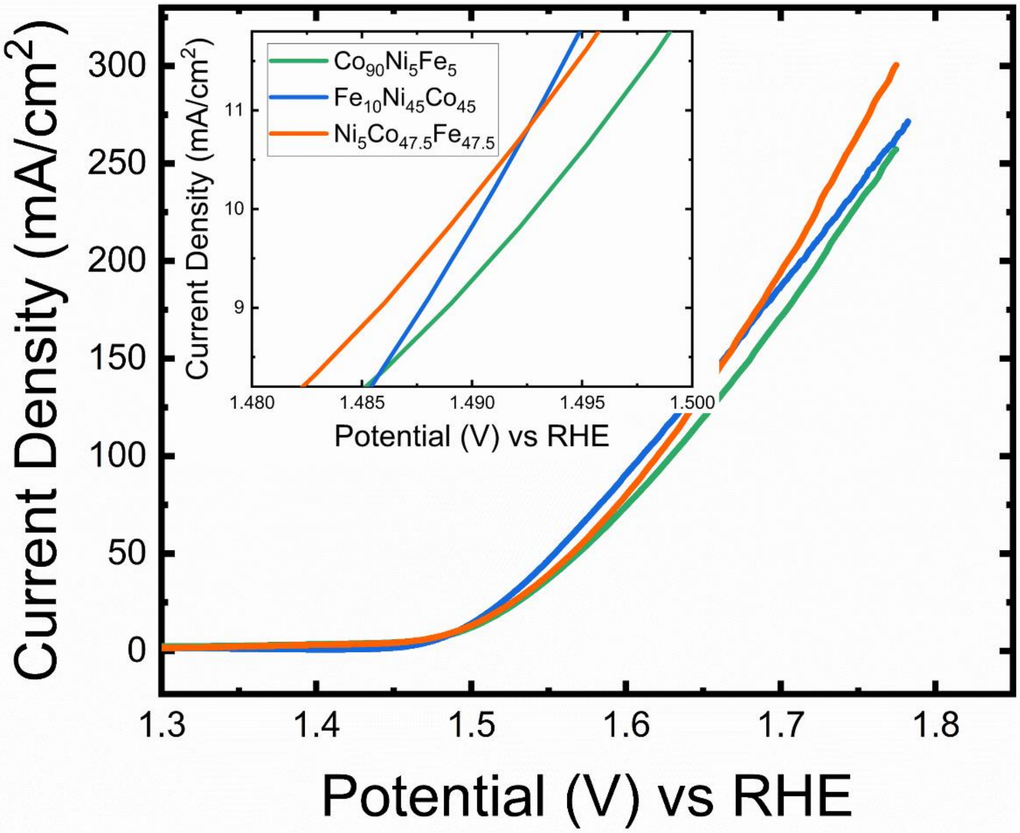

Figure S7: LSV of the best ternary MOF of each family showing superior activity of Ni$_5$Co$_{47.5}$Fe$_{47.5}$ at 10 mA/cm^2. Activity changes with applies current, as Fe$_{10}$Ni$_{45}$Co$_{45}$ shows the best activity at 100 mA/cm^2.

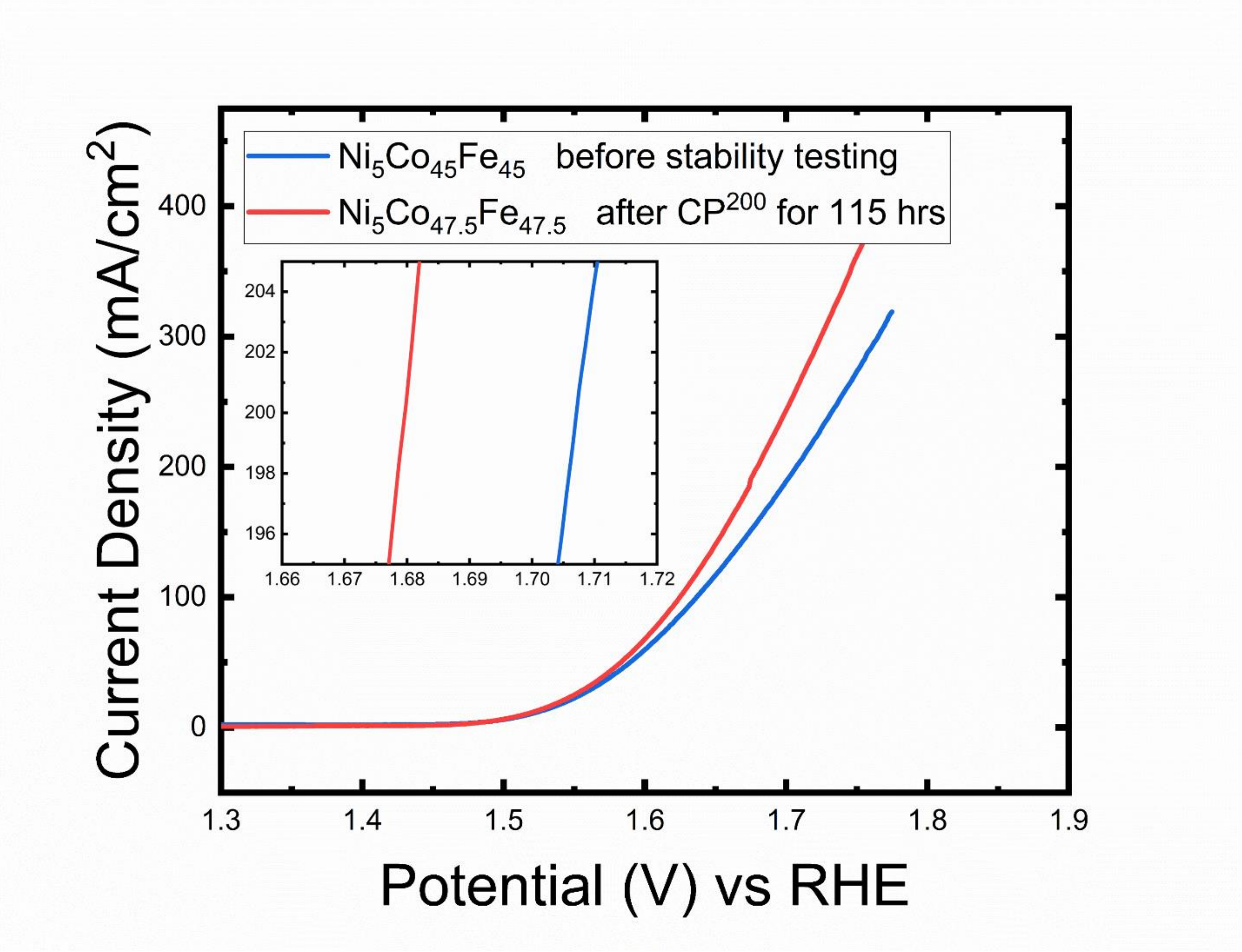

Figure S8: LSV scans before and after stability testing of $Ni_5Co_{47.5}Fe_{47.5}$, with inset showing the difference in potential at 200 mA/cm^2 current density, where samples' overpotential was reduced by 28 mV. at constant current of 200 mA/cm^2. Stability testing was carried out in 1 M KOH for 115 hours under constant current mode of 200 mA/cm^2.

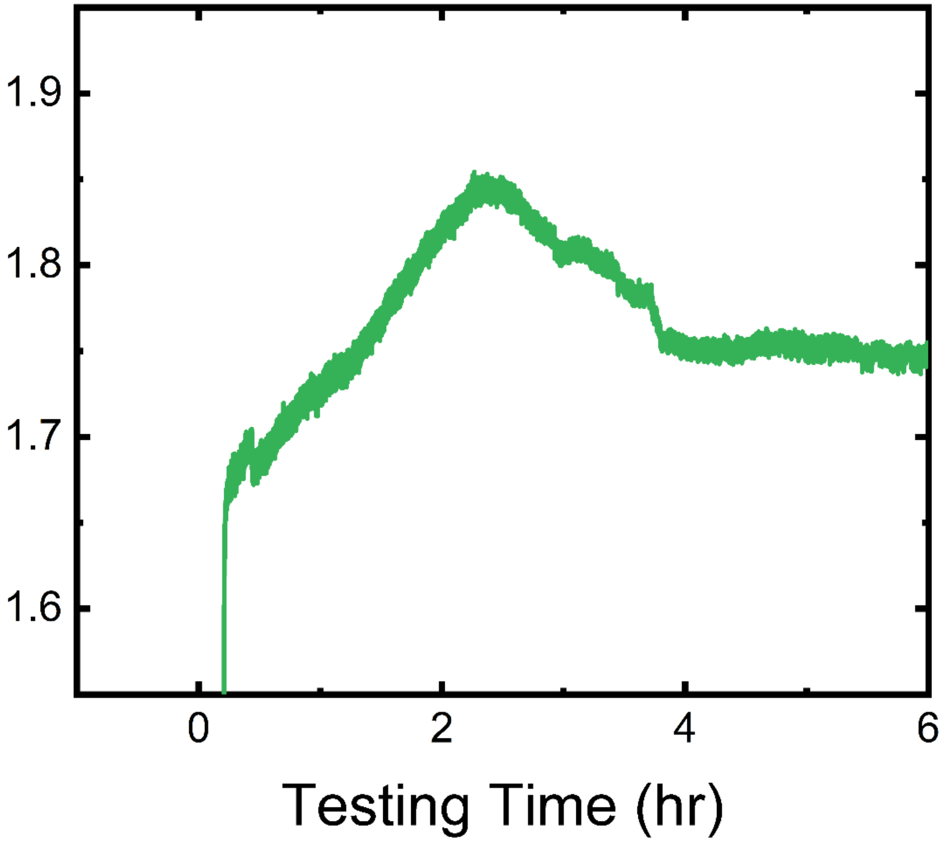

Figure S9: Potential profile of $Fe_{10}Ni_{45}Co_{45}$ sample during the first 6 hours of stability testing at constant current mode of 200 mA/cm^2 (CP200).

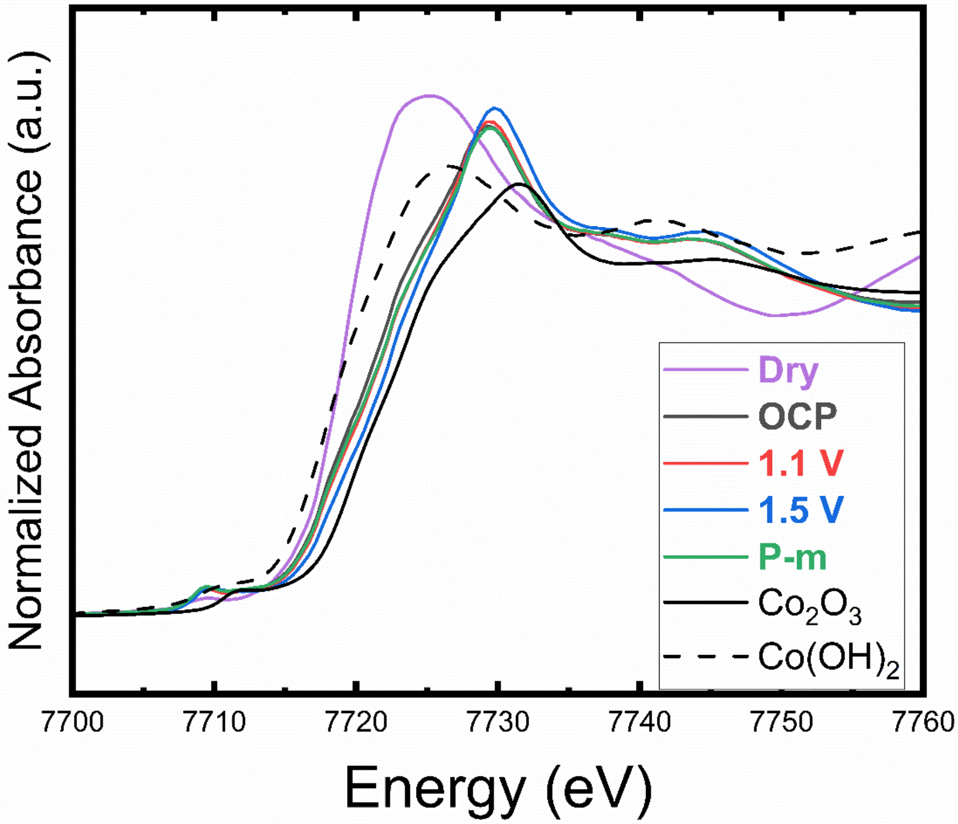

Figure S10: Co K-edge XANES spectra of tri-metallic $Ni_{10}Co_{45}Fe_{45}$

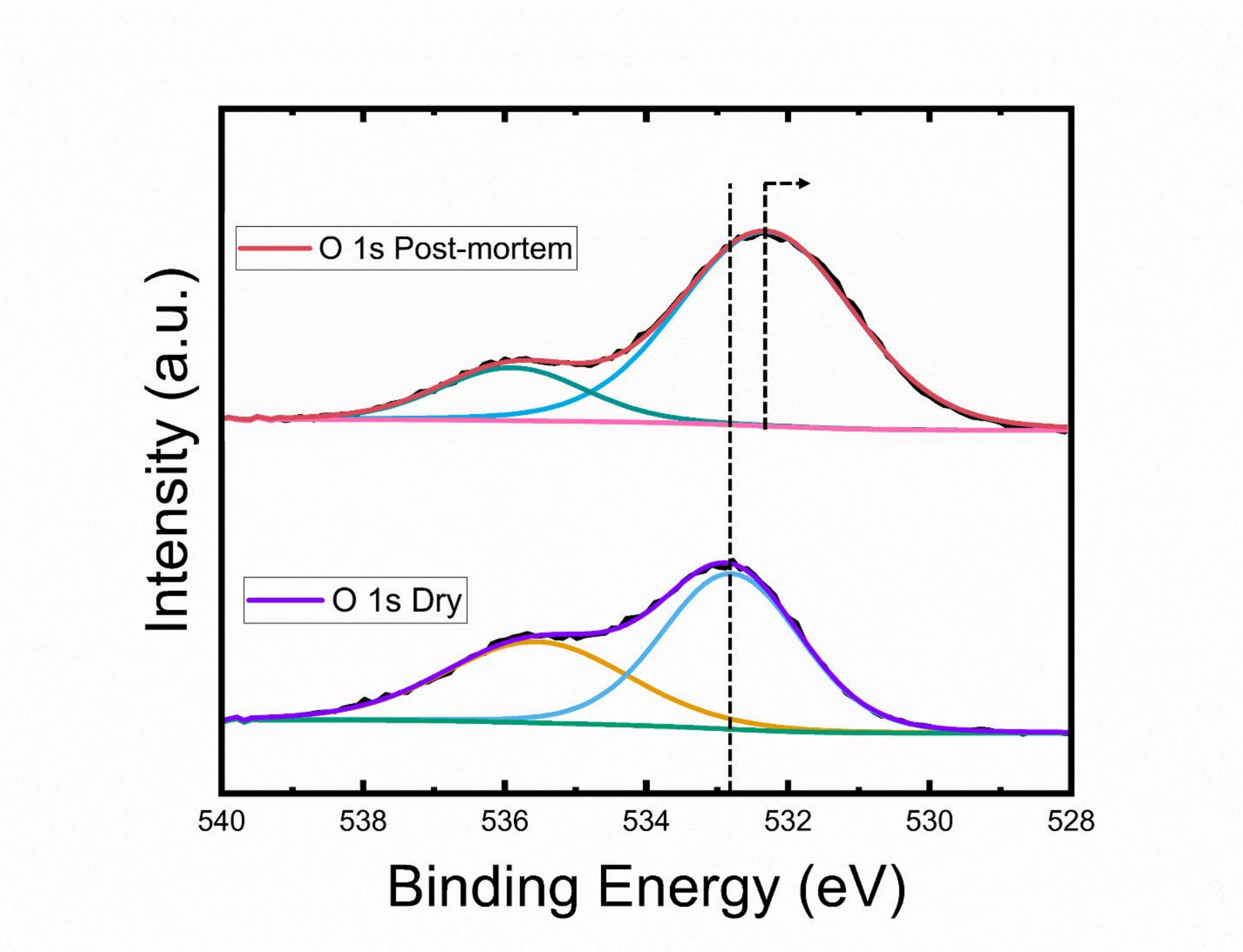

Figure S11: X-ray photoelectron spectroscopy (XPS) spectra of O 1s scans before (dry) and after OER testing (post-mortem), showing significant reduction in O 1s binding energy for post-mortem case by ~0.5 eV

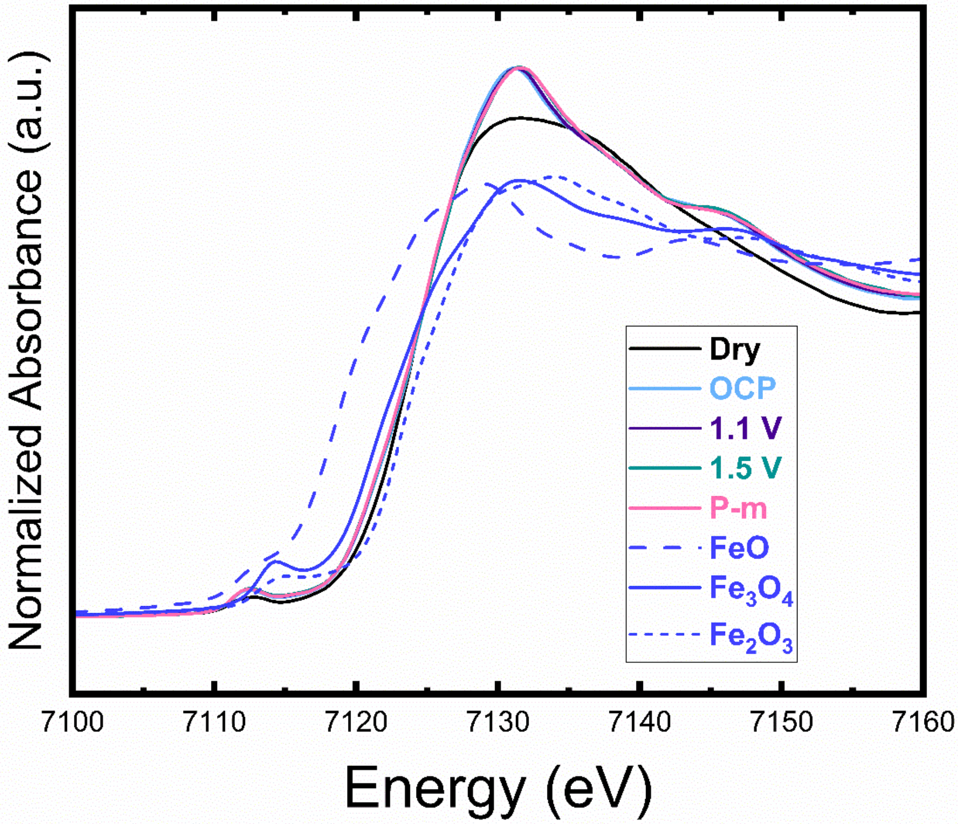

Figure S12: Fe K-edge XANES spectra of tri-metallic $Ni_{10}Co_{45}Fe_{45}$

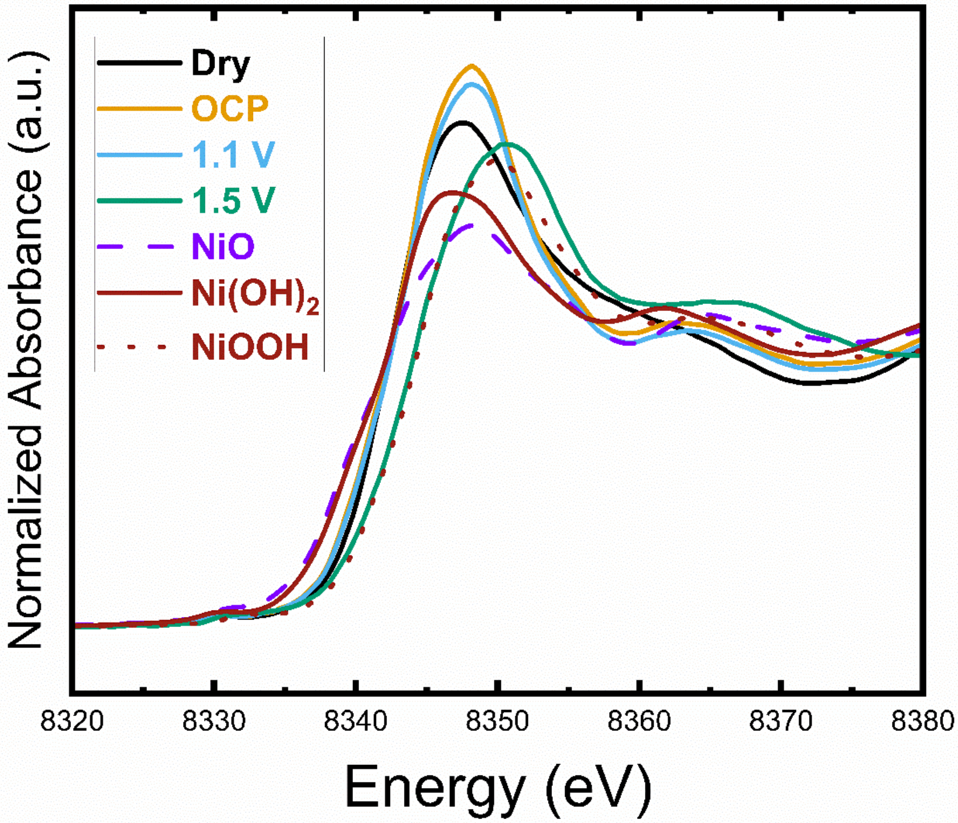

Figure S13: Ni K-edge XANES spectra of tri-metallic $Ni_{10}Co_{45}Fe_{45}$

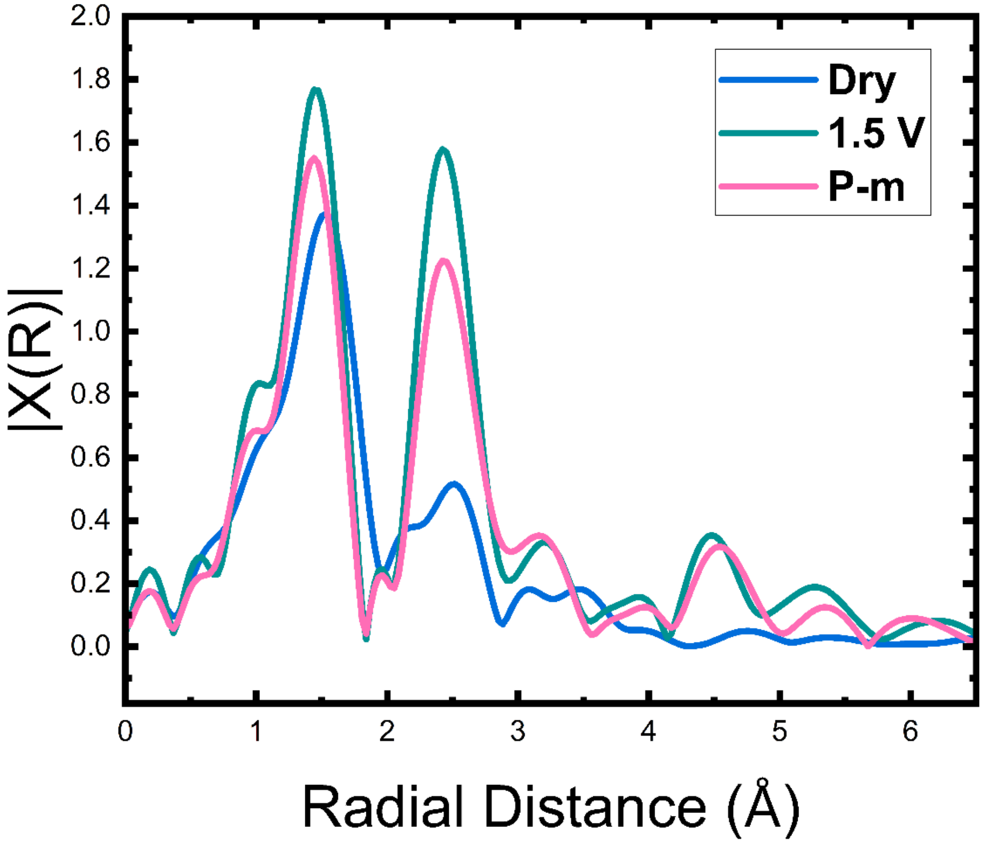

Figure S14: Co K-edge EXAFS spectra of MOF after OER processing, showing an irreversible conversion of the MOF structure after OER, to be completely different from the as-synthesized case.

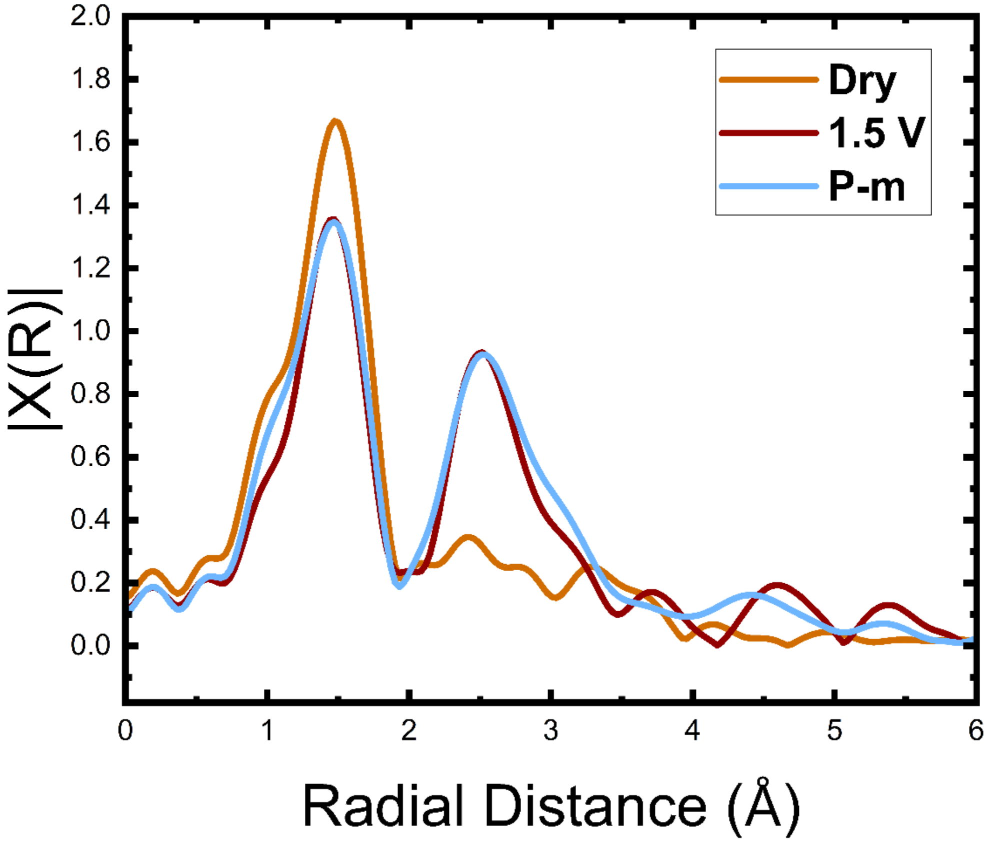

Figure S15: Co K-edge EXAFS spectra of MOF after OER processing, showing an irreversible conversion of the MOF structure after OER, to be completely different from the as-synthesized case.

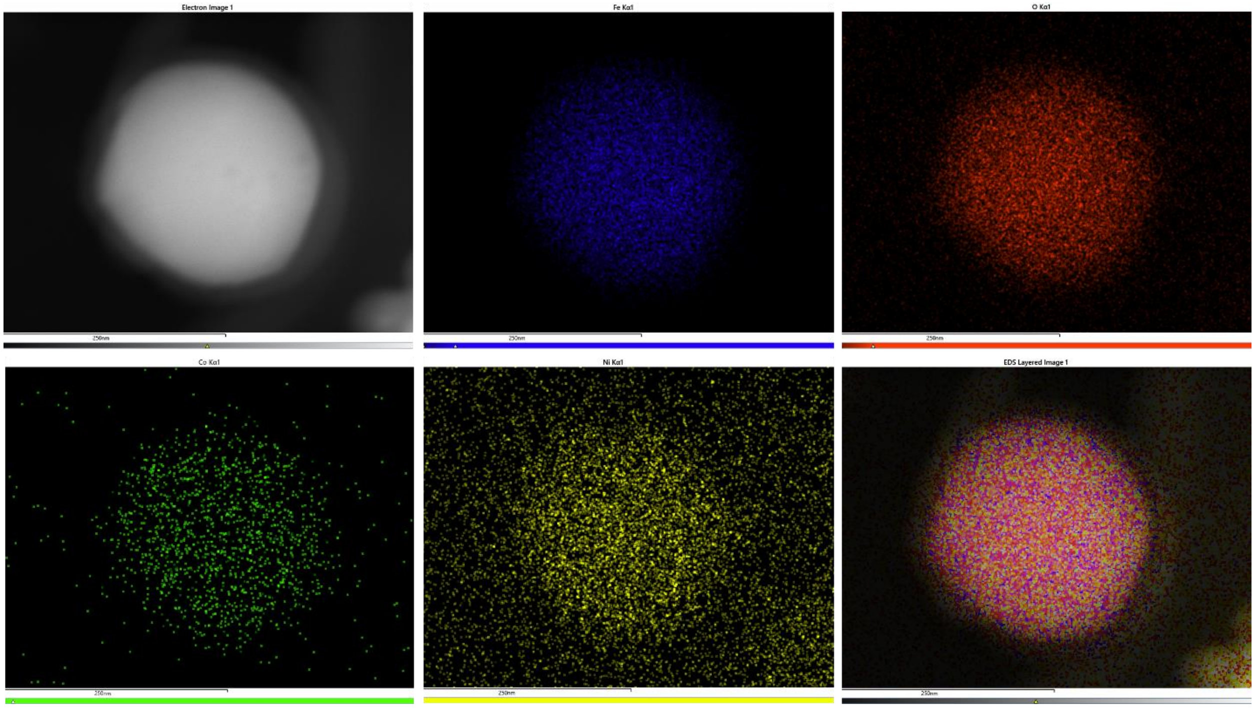

Figure S16: TEM-EDX mapping of tri-metallic MOF supported on Ni-based TEM-grid. Pannels represent TEM image of a MOF particle (top left) and EDX mapping of the different elements (Fe in blue, Oxygen in Red, Co in green, and Ni in yellow) with an overlayed image at the bottom right corner.

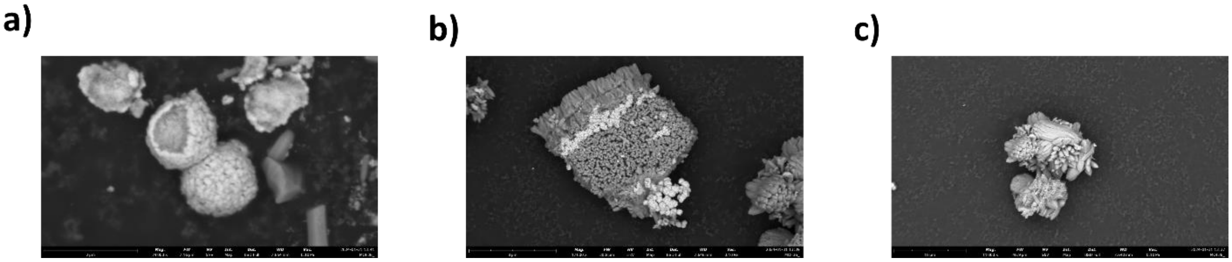

Figure S17: SEM imaging of the as-synthesized MOF showing stacks of MOF particles due to large interfacial interaction of the powder particles with rod-like morphology.

Table S2: Comparing OER performance in alkaline medium of catalysts tested in 3-electrode setup.

Catalyst	Overpotential at 10 mA/cm^2 (mV)	Stability (hr)	Ref
$Fe_{10}Ni_{45}Co_{45}$	**250**	**150 hr @ 200 mA/cm^2**	**This work**
FeNiCo	400	10 hr @ 10mA/cm^2	[17]
FeNiCoCe	357	2hr @ 10 mA/cm^2	[18]
AlNiCoFeMo	260	50 hr @10 mA/cm^2	[19]
FeNiCoCr	221	20 hr @ 10 mA/cm^2	[6]
CoCrFeNiMo	260	24 hr @ 100 mA/cm^2	[20]
LaNiCoCrFeMn	325	50 hr @ 10 mA/cm^2	[21]
$(Cr_{0.2}Mn_{0.2}Fe_{0.2}Co_{0.2}Ni_{0.2})_3O_4$	360	1.5 hr @ 100 mA/cm^2	[22]
CoFeNiCrMn (cited *data is IR-corrected which is usually higher than non-corrected data, such as ours presented herein*)	307	170 hr @ 10 mA/cm^2	[23]
CoCuFeMoOOH@Cu (cited *data is IR-corrected which is usually higher than non-corrected data, such as ours presented herein*)	199	24 hr @ 10 mA/cm^2 24 hr @ 20 mA/cm^2 24 hr @ 50 mA/cm^2	[24]
FeNiCoMoW	233		[25]

Table S3: Comparing OER performance in AEMEC tested in MEA configuration.

Catalyst	Cell Voltage	Stability (hr)	Ref
$Fe_{10}Ni_{45}Co_{45}$	**1.8 V @ 750 mA/cm^2** + **1.9 V @ 1000 mA/cm^2**	**200 hr @ 750 mA/cm^2** + **350 hr @ 1000 mA/cm^2**	**This work**
NiAlMo	2.1 V @ 1000 mA/cm^2	154 hr @ 1000 mA/cm^2	[1]
FexNiyOOH-20F	1.8 V @1020mA/cm^2	70 hr @ 500 mA/cm^2	[2]
$Ni_{0.6}Co_{0.2}Fe_{0.2}$	1.95V @ 500 mA/cm^2	65 hr @ 500 mA/cm^2	[3]
CuCoOx	2 V @ 500mA/cm^2	200 hr @ 500 mA/cm^2	[4]
Ir@Zr–CoP	1.82 V @ 500 mA/cm^2	150 hr @ 500 mA/cm^2	[5]
V-NiFeOOH/Ni3N/NF	1.8 V @ 587 mA/cm^2	192 hr @ 587 mA/cm^2	[6]
NiMo-NH3/H2	1.72 V @ 500 mA/cm^2	25 hr @ 500 mA/cm^2	[7]
RuO2/NiFe	1.71 V @ 500 mA/cm^2	100 hr @ 500 mA/cm^2	[8]